J. Fluid Mech. (2021), *vol*. 909, A1.
Published by Cambridge University Press

doi:10.1017/jfm.2020.853

Consistent lattice Boltzmann model for multicomponent mixtures

N. Sawant[1], **B. Dorschner**[1] **and I. V. Karlin**[1],†

[1]Department of Mechanical and Process Engineering, ETH Zurich, 8092 Zurich, Switzerland

(Received 23 April 2020; revised 7 August 2020; accepted 5 October 2020)

A new lattice Boltzmann model for multicomponent ideal gas mixtures is presented. The model development consists of two parts. First, a new kinetic model for Stefan–Maxwell diffusion amongst the species is proposed and realized as a lattice Boltzmann equation on the standard discrete velocity set. Second, a compressible lattice Boltzmann model for the momentum and energy of the mixture is established. Both parts are consistently coupled through mixture composition, momentum, pressure, energy and enthalpy whereby a passive scalar advection–diffusion coupling is obviated, unlike in previous approaches. The proposed model is realized on the standard three-dimensional lattices and is validated with a set of benchmarks highlighting various physical aspects of compressible mixtures. Stefan–Maxwell diffusion is tested against experiment and theory of uphill diffusion of argon and methane in a ternary mixture with hydrogen. The speed of sound is measured in various binary and ternary compositions. We further validate the Stefan–Maxwell diffusion coupling with hydrodynamics by simulating diffusion in opposed jets and the three-dimensional Kelvin–Helmholtz instability of shear layers in a two-component mixture. Apart from the multicomponent compressible mixture, the proposed lattice Boltzmann model also provides an extension of the lattice Boltzmann equation to the compressible flow regime on the standard three-dimensional lattice.

Key words: kinetic theory

1. Introduction

The lattice Boltzmann method (LBM) is a recast of fluid dynamics into a fully discrete kinetic system of designer particles with the discrete velocities $\boldsymbol{c}_i$, $i = 0, \ldots, Q-1$, fitting into a regular space-filling lattice, with the kinetic equation for the populations $f_i(\boldsymbol{x}, t)$ following a simple algorithm of 'stream along links $\boldsymbol{c}_i$ and collide at the nodes $\boldsymbol{x}$ in discrete time t'. Since its inception (Higuera & Jiménez 1989; Higuera, Succi & Benzi 1989), LBM has evolved into a versatile tool for the simulation of complex flows including transitional flows (Dorschner, Chikatamarla & Karlin 2017), flows in complex moving geometries (Dorschner *et al.* 2016), compressible flows (Yan *et al.* 2013; Frapolli, Chikatamarla & Karlin 2016*b*; Dorschner, Bösch & Karlin 2018; Gan *et al.* 2018; Lin & Luo 2018), multiphase flows (Mazloomi, Chikatamarla & Karlin 2015, 2017;

† Email address for correspondence: ikarlin@ethz.ch

Wöhrwag *et al.* 2018), rarefied gas (Shan, Yuan & Chen 2006) and nanoflow (Montessori *et al.* 2016; Montemore *et al.* 2017), to mention a few recent instances; see Succi (2018), Krüger *et al.* (2017) and Sharma, Straka & Tavares (2020) for a discussion of LBM and its application areas.

In view of extensive development, it seems surprising that the multicomponent gas mixtures so far resisted a significant advancement in the LBM context. Importance of compressible mixtures is hard to overestimate because they are a prerequisite for combustion applications (Williams 1985). However, incorporating the basic mechanism of multicomponent diffusion in gases, the Stefan–Maxwell diffusion, remains an essentially unsolved problem in the LBM context, in spite of the fact that the Stefan–Maxwell diffusion is itself a derivative of Boltzmann's kinetic theory (Chapman & Cowling 1990). It is worth recalling that the Stefan–Maxwell diffusion mechanism is well recognized as a fundamental feature of gas mixtures, supported by experiment (Toor 1957; Duncan & Toor 1962; Arnold & Toor 1967) and molecular dynamics simulations (Wheeler & Newman 2004; Krishna & van Baten 2005). As highlighted by Krishna & Wesselingh (1997), the Stefan–Maxwell diffusion is more subtle than the conventional Fick's model. The latter implies that any component in a mixture moves from higher to lower concentration regions. The Stefan–Maxwell model, on the other hand, accounts for binary interaction between each of the species pairs through pairwise diffusion coefficients and can lead to counter-intuitive effects such as uphill diffusion when a component in a ternary mixture moves from the lower to higher concentration region (Toor 1957; Duncan & Toor 1962; Arnold & Toor 1967). Among applications of Stefan–Maxwell diffusion in the conventional computational fluid dynamics, we mention recent studies of diffusion in fuel cells (Hsing & Futerko 2000; Stockie, Promislow & Wetton 2003; Suwanwarangkul *et al.* 2003). The Stefan–Maxwell diffusion model is more general in comparison with the Fick's diffusion which is strictly valid only for binary mixtures or for the diffusion of a dilute specie in a multicomponent mixture (Krishna & Wesselingh 1997). A comparative study by Suwanwarangkul *et al.* (2003) between the Fick's, dusty-gas and Stefan–Maxwell diffusion models to predict the concentration overpotential in the anode of a solid oxide fuel cell found that the results from the dusty-gas and the Stefan–Maxwell model agree better with the experiment of Yakabe *et al.* (2000). A study of the diffusion in gas diffusion layers of polymer electrolyte membrane fuel cells by Lindstrom & Wetton (2017) found significant difference in the results between the Fick's and the Stefan–Maxwell diffusion models when the anode stream was operated with diluted hydrogen. This led the authors to conclude that modelling with the Stefan–Maxwell diffusion is necessary even though it might complicate a numerical implementation.

To the best of our knowledge, the only LBM realization of the Stefan–Maxwell diffusion was reported recently by Chai *et al.* (2019) and Vienne, Marié & Grasso (2019); although the two-dimensional LBM models of Chai *et al.* (2019) and Vienne *et al.* (2019) differ from one another, they both are restricted by the isothermal and isobaric assumptions and can thus not provide a basis for the development of a compressible mixture LBM. The majority of existing LBM models for the multicomponent mixtures (Chiavazzo *et al.* 2009; Hosseini, Darabiha & Thevenin 2018) are bound to use the Fick diffusion model rather than the Stefan–Maxwell model. Another obstacle arises at the coupling of diffusion to the transport of momentum and energy. The simplest way of tackling multicomponent mixtures with the LBM is by representing the dynamics of the species by an advection–diffusion equation (see, e.g., Chiavazzo *et al.* (2009) and references therein). In this approach, the species are treated as passive scalars, advected with the fluid velocity and the species do not influence the fluid or other species.

The passive scalar viewpoint on LBM for mixtures was recently extended in Hosseini *et al.* (2018, 2020). Apart from the inability of incorporating the Stefan–Maxwell diffusion, the passive scalar approach suffers from a more fundamental shortcoming, namely thermodynamic inconsistency. For example, a conventional passive scalar approach to the energy equation does not readily recover the correct heat flux in the multicomponent system and misses the enthalpy flux due to diffusion (Williams 1985; Chapman & Cowling 1990; Bird, Stewart & Lightfoot 2006). As a remedy, a number of recent works (Feng, Tayyab & Boivin 2018; Hosseini *et al.* 2019; Tayyab *et al.* 2020) abandoned the construction of a kinetic model or LBM for multicomponent mixtures in favour of a so-called hybrid LBM where only the flow of the mixture is represented by an (augmented) LBM equation while the species and the temperature dynamics are modelled by conventional macroscopic equations. While the hybrid LBM approach can be potentially useful, in particular for combustion applications, our goal here is to retain a fully kinetic model and LBM for multicomponent mixtures.

In this paper we revisit the LBM construction for a compressible multicomponent mixture, focusing on a thermodynamically consistent coupling between the Stefan–Maxwell diffusion and momentum and energy transfer in the system. We begin in § 2 with setting up a kinetic system for the species in the M-component mixture. The construction follows the path of so-called quasi-equilibrium kinetic models (Gorban & Karlin 1994; Ansumali *et al.* 2007); see Arcidiacono *et al.* (2007) in the context of isothermal mixtures. Here, we significantly extend the quasi-equilibrium kinetic model for the species to a generic ideal gas equation of state and, unlike in the earlier approach of Arcidiacono *et al.* (2007), enabling the Stefan–Maxwell constitutive relation. After a short summary of nomenclature in § 2.1, the species kinetic equations are introduced in § 2.2, in the continuous time–space setting. We show in § 2.3 that the proposed kinetic equations recover the Stefan–Maxwell diffusion together with the barodiffusion in the hydrodynamic limit. The species kinetic equations are realized on the standard set of discrete velocities in § 2.4. In § 2.5 we derive the lattice Boltzmann scheme for the species kinetic equations following the technique of integration along characteristics introduced by He, Chen & Doolen (1998). This concludes the first part of the model development. In addition, while the Stefan–Maxwell exact diffusion relation is the main concern of our study, in appendix A we show how other approximate diffusion models such as Curtiss–Hirschfelder and generalized Fick (Kee, Coltrin & Glarborg 2003; Poinsot & Veynante 2005; Giovangigli 2012) are derived from our kinetic model. We continue in § 3 with a mean-field lattice Boltzmann formulation of the mixture momentum and energy. After a summary on the mixture energy and enthalpy of a generic non-reactive mixture in § 3.1, we present a two-population lattice Boltzmann equation for the mixture. We note that the mean-field approach requires only two lattice Boltzmann equations, one for the mixture density and momentum and another one for the energy. While the two-population LBM is an established approach for a single-component compressible fluid (Frapolli, Chikatamarla & Karlin 2015; Saadat, Bösch & Karlin 2019), the application of the two-population techniques to the mixture requires a modification of the non-equilibrium fluxes discussed in § 3.2. The mixture density, momentum and energy equations are presented in § 3.3, while details of their derivation with the Chapman–Enskog analysis (Chapman & Cowling 1990) are summarized in the appendix B. The two-population mixture LBM is realized on the standard lattice in § 3.4 where we extend the two-dimensional compressible LBM of Saadat *et al.* (2019) to three-dimensional mixtures. Finally, in § 3.5 we discuss the coupling between the M LBM equations for the species and the double-population mean-field mixture LBM. The resulting LBM provides a reduced description of the M-component

mixture with $M + 2$ tightly coupled lattice Boltzmann equations, unlike a standard kinetic approach which would require $2 \times M$ kinetic equations.

In § 4 the LBM model is validated with a number of select benchmarks. After a summary of general aspects of numerical implementation in § 4.1, we present a simulation of diffusion of argon and methane ternary mixtures with hydrogen in the Loschmidt tube apparatus in § 4.2, along with the classical experiment of Arnold & Toor (1967) and theoretical discussion of Krishna & Wesselingh (1997). We show that the LBM simulations reproduce in a quantitative fashion the experimentally observed features of the Stefan–Maxwell diffusion such as uphill and osmotic diffusion and the diffusion barrier (Toor 1957; Duncan & Toor 1962; Arnold & Toor 1967; Krishna & Wesselingh 1997). The coupling between hydrodynamics and diffusion is validated in a counterflow diffusion in opposed jets in § 4.3 and the speed of sound measurements are presented in § 4.4 for probing the compressible flow aspect of the model. Finally, a simulation of the three-dimensional Kelvin–Helmholtz instability in a binary mixture is reported in § 4.5 as a test for the performance of the proposed LBM in a complex flow. Conclusions are drawn in § 5.

2. Lattice Boltzmann model of Stefan–Maxwell diffusion

2.1. *Composition and equation of state of ideal gas mixture*

We begin with introducing some nomenclature and notation. Let us consider a mixture composed of M ideal gases. The composition is described by the species densities ρ_a, $a = 1, \ldots, M$, while the mixture density is

$$\rho = \sum_{a=1}^{M} \rho_a. \tag{2.1}$$

Equivalently, the mixture composition is defined by the mixture density ρ and the $M - 1$ independent mass fractions Y_a,

$$Y_a = \frac{\rho_a}{\rho}, \quad \sum_{a=1}^{M} Y_a = 1. \tag{2.2a,b}$$

With the molar mass of the component m_a, the mean molar mass m depends on the composition,

$$\frac{1}{m} = \sum_{a=1}^{M} \frac{Y_a}{m_a}. \tag{2.3}$$

The equation of state provides a relation between the pressure P, the temperature T and the composition,

$$P = \rho R T. \tag{2.4}$$

Here, R is the specific gas constant that contains the information about the composition of the gas by way of the mean molar mass m,

$$R = \frac{R_U}{m}, \tag{2.5}$$

where $R_U \approx 8.314$ kJ K^{-1} $\cdot$ kmol^{-1} is the universal gas constant. Thus, for a mixture of ideal gases, the specific gas constant R is a function of local composition and changes in

space and time. The pressure of an individual component P_a is related to the pressure of the mixture P through Dalton's law of partial pressures as

$$P_a = X_a P, \tag{2.6}$$

where the mole fraction of a component X_a is related to its mass fraction Y_a as

$$X_a = \left(\frac{m}{m_a}\right) Y_a, \quad \sum_{a=1}^{M} X_a = 1. \tag{2.7a,b}$$

A consequence of Dalton's law of partial pressure is that $\sum_{a=1}^{M} P_a = P$. Combined with the equation of state (2.4), the partial pressure P_a takes the form

$$P_a = \rho_a R_a T, \tag{2.8}$$

where R_a is the specific gas constant of the component,

$$R_a = \frac{R_U}{m_a}. \tag{2.9}$$

With these thermodynamic relations in mind, we proceed to setting up the kinetic equations that recover the Stefan–Maxwell diffusion in the macroscopic limit.

2.2. *Kinetic equation for the species*

In this section we set-up kinetic equations which recover the Stefan–Maxwell diffusion model for an M-component ideal gas mixture. Each component is described by a set of populations f_{ai}, $a = 1, \ldots, M$, corresponding to the discrete velocities $\boldsymbol{c}_i$, $i = 0, \ldots, Q-1$. The proposed kinetic equation for each of the species a is written as

$$\partial_t f_{ai} + \boldsymbol{c}_i \cdot \nabla f_{ai} = \sum_{b \neq a}^{M} \frac{1}{\theta_{ab}} \left[\left(\frac{f_{ai}^{eq} - f_{ai}}{\rho_a} \right) - \left(\frac{f_{bi}^{eq} - f_{bi}^{*}}{\rho_b} \right) \right]. \tag{2.10}$$

Here, ρ_a is the density of the component a, which is defined as the zeroth moment of populations f_{ai},

$$\rho_a = \sum_{i=0}^{Q-1} f_{ai}. \tag{2.11}$$

Furthermore, a symmetric set of relaxation parameters $\theta_{ab} = \theta_{ba}$ shall be related to the binary diffusion coefficients in the following. The equilibrium f_{ai}^{eq} and the quasi-equilibrium f_{ai}^{*} populations will be fully defined in § 2.4. Here, we only need to specify the conditions for the low-order moments thereof. To that end, let us introduce the

partial momenta $\rho_a \boldsymbol{u}_a$ as first moments of the species' populations,

$$\rho_a \boldsymbol{u}_a = \sum_{i=0}^{Q-1} f_{ai} \boldsymbol{c}_i. \tag{2.12}$$

The quasi-equilibrium populations f_{ai}^* must satisfy the following set of constraints,

$$\sum_{i=0}^{Q-1} f_{ai}^* = \rho_a, \tag{2.13}$$

$$\sum_{i=0}^{Q-1} f_{ai}^* \boldsymbol{c}_i = \rho_a \boldsymbol{u}_a. \tag{2.14}$$

The momenta of the components sum up to the mixture momentum,

$$\sum_{a=1}^{M} \rho_a \boldsymbol{u}_a = \rho \boldsymbol{u}. \tag{2.15}$$

The equilibrium populations f_{ai}^{eq} have to verify the following set of constraints:

$$\sum_{i=0}^{Q-1} f_{ai}^{eq} = \rho_a, \tag{2.16}$$

$$\sum_{i=0}^{Q-1} f_{ai}^{eq} \boldsymbol{c}_i = \rho_a \boldsymbol{u}, \tag{2.17}$$

$$\sum_{i=0}^{Q-1} f_{ai}^{eq} \boldsymbol{c}_i \otimes \boldsymbol{c}_i = P_a \boldsymbol{I} + \rho_a \boldsymbol{u} \otimes \boldsymbol{u}. \tag{2.18}$$

In (2.18) the partial pressure P_a (2.8) depends on the temperature T, which is obtained from the mixture kinetic equations of § 3. Finally, the quasi-equilibrium distribution must match the equilibrium if the species velocity equals the velocity of the mixture, $\boldsymbol{u}_a = \boldsymbol{u}$:

$$f_{ai}^*(\boldsymbol{u}_a)|_{\boldsymbol{u}_a = \boldsymbol{u}} = f_{ai}^{eq}(\boldsymbol{u}). \tag{2.19}$$

Some comments are in order.

(i) The M-component kinetic system satisfies $M + D$ conservation laws, where D is the space dimension: the densities $\rho_1, \ldots, \rho_M$ and the vector of fluid momentum $\rho \boldsymbol{u}$ are locally conserved fields.
(ii) Thanks to the matching condition (2.19), the relaxation term on the right-hand side of (2.10) vanishes only at the equilibrium.

We now proceed with the identification of the relaxation parameters θ_{ab} in terms of the Stefan–Maxwell binary diffusion coefficients.

2.3. *Hydrodynamic limit of kinetic equations for the species*

Evaluation of the zeroth and first moments of the kinetic equation (2.10) results in the balance equations for the species densities and species velocities,

$$\partial_t \rho_a = -\nabla \cdot (\rho_a \boldsymbol{u}_a), \tag{2.20}$$

$$\rho_a \partial_t \boldsymbol{u}_a = \boldsymbol{u}_a \nabla \cdot (\rho_a \boldsymbol{u}_a) - \nabla \cdot \boldsymbol{P}_a + \sum_{b \neq a}^{M} \frac{1}{\theta_{ab}} (\boldsymbol{u}_b - \boldsymbol{u}_a). \tag{2.21}$$

Here, $\boldsymbol{P}_a$ is the partial pressure tensor,

$$\boldsymbol{P}_a = \sum_{i=0}^{Q-1} f_{ai} \boldsymbol{c}_i \otimes \boldsymbol{c}_i. \tag{2.22}$$

Upon summation over the components in (2.20), we arrive at the continuity equation for the mixture density,

$$\partial_t \rho = -\nabla \cdot (\rho \boldsymbol{u}), \tag{2.23}$$

while the summation over components in (2.21) results in the mixture momentum balance,

$$\partial_t (\rho \boldsymbol{u}) = -\nabla \cdot \boldsymbol{P}, \tag{2.24}$$

where $\boldsymbol{P}$ is the mixture pressure tensor,

$$\boldsymbol{P} = \sum_{a=1}^{M} \boldsymbol{P}_a. \tag{2.25}$$

The low-order closure relation for the species balance equation (2.20) is established by considering a perturbation around the equilibrium,

$$\boldsymbol{u}_a = \boldsymbol{u} + \delta \boldsymbol{u}_a, \tag{2.26}$$

where the perturbation $\delta \boldsymbol{u}_a$ satisfies the consistency condition,

$$\sum_{a=1}^{M} \rho_a \delta \boldsymbol{u}_a = 0. \tag{2.27}$$

To first order, upon substitution into (2.21), we get the constitutive relation for the diffusion velocity $\delta \boldsymbol{u}_a$,

$$\rho_a \partial_t \boldsymbol{u} - \boldsymbol{u} \nabla \cdot (\rho_a \boldsymbol{u}) + \nabla \cdot \boldsymbol{P}_a^{eq} = \sum_{b \neq a}^{M} \frac{1}{\theta_{ab}} (\delta \boldsymbol{u}_b - \delta \boldsymbol{u}_a). \tag{2.28}$$

Upon summation over the species, and by taking into account Dalton's law in the equilibrium pressure tensor (2.18), the compressible Euler equation for the flow velocity

is established,

$$\partial_t \boldsymbol{u} = -\boldsymbol{u}\cdot\nabla\boldsymbol{u} - \frac{1}{\rho}\nabla P. \tag{2.29}$$

By elimination of the time derivative in (2.28), we get the constitutive relation as

$$P\nabla X_a + (X_a - Y_a)\nabla P = \sum_{b\neq a}^{M} \frac{1}{\theta_{ab}}(\delta\boldsymbol{u}_b - \delta\boldsymbol{u}_a). \tag{2.30}$$

Constitutive relation (2.30) becomes the Stefan–Maxwell diffusion equation once the relaxation parameters θ_{ab} are identified in terms of the binary diffusion coefficients $\mathcal{D}_{ab}$ as

$$\theta_{ab} = \frac{\mathcal{D}_{ab}}{PX_aX_b}. \tag{2.31}$$

Summarizing, kinetic equations for the species (2.10) recover the Stefan–Maxwell law of diffusion in the hydrodynamic limit, with both the diffusion due to non-uniformity of the species molar concentration and the barodiffusion taken into account. The present model does not include thermodiffusion as it should be expected by the simplicity of the relaxation term. We comment that the above derivation of (2.30) assumes the validity of the equation of state. The latter, in turn, depends on the temperature derived from the mixture energy equation, and which shall be introduced in § 3. We now proceed with finalizing the continuous time–space kinetic equations by identifying the equilibrium and the quasi-equilibrium populations.

2.4. *Realization on the standard lattice*

The above kinetic model is realized on the standard three-dimensional $D3Q27$ lattice, where $D = 3$ stands for three dimensions and $Q = 27$ is the number of discrete velocities:

$$\boldsymbol{c}_i = (c_{ix}, c_{iy}, c_{iz}), \quad c_{i\alpha} \in \{-1, 0, 1\}. \tag{2.32a,b}$$

Following Karlin & Asinari (2010) we define a triplet of functions in two variables, ξ and $\zeta > 0$,

$$\Psi_0(\xi,\zeta) = 1 - (\xi^2 + \zeta), \quad \Psi_1(\xi,\zeta) = \frac{\xi + (\xi^2+\zeta)}{2}, \quad \Psi_{-1}(\xi,\zeta) = \frac{-\xi + (\xi^2+\zeta)}{2}. \tag{2.33a–c}$$

For a vector $\boldsymbol{\xi} = (\xi_x, \xi_y, \xi_z)$, we consider a product form associated with the discrete velocities $\boldsymbol{c}_i$ (2.32*a*,*b*),

$$\Psi_i(\boldsymbol{\xi},\zeta) = \Psi_{c_{ix}}(\xi_x,\zeta)\Psi_{c_{iy}}(\xi_y,\zeta)\Psi_{c_{iz}}(\xi_z,\zeta). \tag{2.34}$$

The equilibrium f_{ai}^{eq} and the quasi-equilibrium f_{ai}^{*} are represented with the product form (2.34) by choosing $\boldsymbol{\xi} = \boldsymbol{u}$ or $\boldsymbol{\xi} = \boldsymbol{u}_a$, respectively, and by assigning $\zeta = R_aT$ in both cases:

$$f_{ai}^{eq}(\rho_a, \boldsymbol{u}, R_aT) = \rho_a\Psi_{c_{ix}}(u_x, R_aT)\Psi_{c_{iy}}(u_y, R_aT)\Psi_{c_{iz}}(u_z, R_aT), \tag{2.35}$$

$$f_{ai}^{*}(\rho_a, \boldsymbol{u}_a, R_aT) = \rho_a\Psi_{c_{ix}}(u_{ax}, R_aT)\Psi_{c_{iy}}(u_{ay}, R_aT)\Psi_{c_{iz}}(u_{az}, R_aT). \tag{2.36}$$

One can readily verify that, the equilibrium (2.35) and the quasi-equilibrium (2.36) satisfy all the constraints put forward in § 2.2. We now proceed with the lattice Boltzmann discretization of the kinetic equations (2.10).

2.5. *Lattice Boltzmann equation for the species*

2.5.1. *Kinetic equations in the relaxation form*

With the mass diffusivity (2.31), the kinetic equation (2.10) is written as

$$\partial_t f_{ai} + \boldsymbol{c}_i \cdot \boldsymbol{\nabla} f_{ai} = \sum_{b\neq a}^{M} \frac{P X_a X_b}{\mathcal{D}_{ab}} \left[\left(\frac{f_{ai}^{eq} - f_{ai}}{\rho_a} \right) - \left(\frac{f_{bi}^{eq} - f_{bi}^{*}}{\rho_b} \right) \right]. \tag{2.37}$$

It can readily be seen that, in its present form, (2.37) is not well suited for numerical implementation. Indeed, in an actual problem, the density of some species can be small or even vanishing if a particular gas component is absent at some location. This is an inconvenience rather than a failure since vanishing of the density is compensated by the simultaneously vanishing molar fraction in the product $X_a X_b$. Hence, we first transform (2.37) in order to eliminate this artifact. Substituting the equation of state (2.4) into (2.37), we get

$$\partial_t f_{ai} + \boldsymbol{c}_i \cdot \boldsymbol{\nabla} f_{ai} = \sum_{b\neq a}^{M} \left(\frac{m}{m_a m_b} \right) \left(\frac{R_U T}{\mathcal{D}_{ab}} \right) [Y_b (f_{ai}^{eq} - f_{ai}) - Y_a (f_{bi}^{eq} - f_{bi}^{*})]. \tag{2.38}$$

Equation (2.38) is equivalent to (2.37) and does not suffer from a spurious division by a vanishing density. Furthermore, it proves convenient to recast (2.38) in a relaxation form. To that end, let us define characteristic times $\tau_{ab} = \tau_{ba}$,

$$\frac{1}{\tau_{ab}} = \left(\frac{R_U T}{\mathcal{D}_{ab}} \right) \left(\frac{m}{m_a m_b} \right), \tag{2.39}$$

and let us introduce the relaxation times τ_a,

$$\frac{1}{\tau_a} = \sum_{b\neq a}^{M} \frac{Y_b}{\tau_{ab}} = R_a T \left(\sum_{b\neq a}^{M} \frac{X_b}{\mathcal{D}_{ab}} \right). \tag{2.40}$$

Finally, let us introduce a shorthand notation,

$$F_{ai} = Y_a \sum_{b\neq a}^{M} \frac{1}{\tau_{ab}} (f_{bi}^{eq} - f_{bi}^{*}). \tag{2.41}$$

With these definitions, the kinetic equation (2.38) can be rearranged as follows:

$$\partial_t f_{ai} + \boldsymbol{c}_i \cdot \boldsymbol{\nabla} f_{ai} = \frac{1}{\tau_a} (f_{ai}^{eq} - f_{ai}) - F_{ai}. \tag{2.42}$$

The species kinetic equations (2.42) are now cast into the relaxation form, familiar from previous lattice Boltzmann models. The right-hand side comprises the conventional relaxation term and a source term (2.41). The latter depends on the populations only through the local densities, momenta and the temperature, as prescribed by the local equilibrium and quasi-equilibrium populations (2.35) and (2.36). Hence, kinetic equation (2.42) is amenable to a lattice Boltzmann discretization in time and space.

2.5.2. *Derivation of the lattice Boltzmann equation*

Following a procedure first introduced by He *et al.* (1998), we integrate (2.42) along the characteristics and apply the trapezoidal rule on the right-hand side to obtain

$$f_{ai}(\boldsymbol{x}+\boldsymbol{c}_i\delta t, t+\delta t) - f_{ai}(\boldsymbol{x}, t) = \frac{\delta t}{2\tau_a}[f_{ai}^{eq}(\boldsymbol{x}+\boldsymbol{c}_i\delta t, t+\delta t) - f_{ai}(\boldsymbol{x}+\boldsymbol{c}_i\delta t, t+\delta t)] + \frac{\delta t}{2\tau_a}[f_{ai}^{eq}(\boldsymbol{x}, t) - f_{ai}(\boldsymbol{x}, t)] - \frac{\delta t}{2}F_{ai}(\boldsymbol{x}+\boldsymbol{c}_i\delta t, t+\delta t) - \frac{\delta t}{2}F_{ai}(\boldsymbol{x}, t). \tag{2.43}$$

Next, we introduce transformed populations k_{ai},

$$f_{ai} = k_{ai} + \frac{\delta t}{2\tau_a}(f_{ai}^{eq} - f_{ai}) - \frac{\delta t}{2}F_{ai}. \tag{2.44}$$

Let us evaluate the pertinent moments of the transform (2.44). Summation over the discrete velocities gives

$$\rho_a(f) = \rho_a(k), \tag{2.45}$$

where we have specified that the density $\rho_a(f)$ on the left-hand side is defined using the original populations f_{ai} while the density $\rho_a(k)$ is defined by the zeroth moment of the k-populations,

$$\rho_a(k) = \sum_{i=0}^{Q-1} k_{ai}. \tag{2.46}$$

Thus, the species densities do not alter under the populations transformation, and the specification can be dropped: $\rho_a = \rho_a(f) = \rho_a(k)$. On the other hand, evaluating the first moment of (2.44) gives

$$\rho_a\boldsymbol{u}_a(f)\left(1+\frac{\delta t}{2\tau_a}\right) - \frac{\delta t}{2}Y_a\sum_{b\neq a}^{M}\frac{1}{\tau_{ab}}\rho_b\boldsymbol{u}_b(f) = \rho_a\boldsymbol{u}_a(k), \tag{2.47}$$

where the species velocity $\boldsymbol{u}_a(k)$ is defined by the k-populations in a conventional way,

$$\rho_a\boldsymbol{u}_a(k) = \sum_{i=0}^{Q-1} k_{ai}\boldsymbol{c}_i. \tag{2.48}$$

Summation over the species in (2.47) shows that the momentum $\rho\boldsymbol{u}$ is also an invariant of the transform (2.44):

$$\rho\boldsymbol{u}(f) = \rho\boldsymbol{u}(k). \tag{2.49}$$

Since the term F_{ai} vanishes at equilibrium, and also thanks to the invariance of the local conservation (2.45) and (2.49), the equilibrium is the fixed point of the map (2.44):

$$f_{ai}^{eq}(\rho_a, \boldsymbol{u}, R_aT) = k_{ai}^{eq}(\rho, \boldsymbol{u}, R_aT). \tag{2.50}$$

Substituting (2.44) into (2.43), and introducing the parameters $\beta_a \in [0, 1]$,

$$\beta_a = \frac{\delta t}{2\tau_a + \delta t}, \tag{2.51}$$

we get

$$k_{ai}(\boldsymbol{x}+\boldsymbol{c}_i\delta t, t+\delta t) = k_{ai}(\boldsymbol{x}, t) + 2\beta_a[k_{ai}^{eq}(\boldsymbol{x}, t) - k_{ai}(\boldsymbol{x}, t)] + \delta t(\beta_a - 1)F_{ai}(\boldsymbol{x}, t). \quad (2.52)$$

The last term in (2.52) is spelled out as follows. The quasi-equilibrium population f_{ai}^* in the expression F_{ai} (2.41) depends on the species velocity $\boldsymbol{u}_a(f)$. The latter, unlike the mixture velocity $\boldsymbol{u}(f)$ (2.49), is not invariant under the transform to the k-populations. Rather, $\boldsymbol{u}_a(f)$ has to be evaluated using the linear relation (2.47) in terms of $\boldsymbol{u}_b(k)$ by solving a $M \times M$ linear system for each of the spatial components. In our realization we used Gauss elimination.

2.5.3. *Summary of the lattice Boltzmann equation for the Stefan–Maxwell diffusion*

For convenience, we summarize the lattice Boltzmann equation for the species. We return to a more conventional notation and rename k_{ai} to f_{ai} in (2.52),

$$f_{ai}(\boldsymbol{x}+\boldsymbol{c}_i\delta t, t+\delta t) - f_{ai}(\boldsymbol{x}, t) = 2\beta_a[f_{ai}^{eq} - f_{ai}] + \delta t(\beta_a - 1)F_{ai}. \quad (2.53)$$

The last term is written as

$$F_{ai} = Y_a \sum_{b\neq a}^{M} \left(\frac{R_U T}{\mathcal{D}_{ab}}\right)\left(\frac{m}{m_a m_b}\right)[f_{bi}^{eq}(\rho_b, \boldsymbol{u}, R_b T) - f_{bi}^{*}(\rho_b, \boldsymbol{u}+\boldsymbol{V}_b, R_b T)], \quad (2.54)$$

where we have introduced the transformed diffusion velocities of the components, $\boldsymbol{V}_a$, $a = 1, \ldots, M$. The latter are defined by (2.47) which can be recast as follows:

$$\rho_a \boldsymbol{V}_a - \left(\frac{\delta t}{2}\right)\sum_{b\neq a}^{M} \frac{P X_a X_b}{\mathcal{D}_{ab}}[\boldsymbol{V}_b - \boldsymbol{V}_a] = \rho_a(\boldsymbol{u}_a - \boldsymbol{u}). \quad (2.55)$$

The field $\rho_a \boldsymbol{u}_a$ on the right-hand side of (2.55) is defined by the moment relation as before,

$$\rho_a \boldsymbol{u}_a = \sum_{i=0}^{Q-1} f_{ai}\boldsymbol{c}_i. \quad (2.56)$$

The $M + D$ independent conservation laws of the M-component system (2.53) correspond to the mass of each component and the momentum of the mixture. The corresponding locally conserved fields are the species densities ρ_a and the momentum flux $\rho\boldsymbol{u}$,

$$\rho_a = \sum_{i=0}^{Q-1} f_{ai}, \quad (2.57)$$

$$\rho\boldsymbol{u} = \sum_{a=1}^{M} \rho_a \boldsymbol{u}_a = \sum_{a=1}^{M}\sum_{i=0}^{Q-1} f_{ai}\boldsymbol{c}_i. \quad (2.58)$$

The conservation law of the fluid mass is the implication of the mass conservation of each component. The density of the mixture ρ is defined by the densities of the components,

$$\rho = \sum_{a=1}^{M} \rho_a = \sum_{a=1}^{M}\sum_{i=0}^{Q-1} f_{ai}, \quad (2.59)$$

while the flow velocity $\boldsymbol{u}$ is

$$\boldsymbol{u} = \frac{\rho \boldsymbol{u}}{\rho} = \frac{\sum_{a=1}^{M} \sum_{i=0}^{Q-1} f_{ai} \boldsymbol{c}_i}{\sum_{a=1}^{M} \sum_{i=0}^{Q-1} f_{ai}}. \tag{2.60}$$

Finally, we recall that the temperature dependence in the equilibrium and in the quasi-equilibrium populations has to be supplied by the energy equation to be discussed in the next section.

The Stefan–Maxwell diffusion relation is a source of a variety of approximate constitutive relations for the multicomponent diffusion where the former is substituted by a simpler, often explicit expression. Diffusion models such as the mixture averaged approximation are widely used; see, e.g., Giovangigli (2012), Williams (1985), Poinsot & Veynante (2005), Kee *et al.* (2003) and Bird *et al.* (2006). In appendix A we show how approximate constitutive relations are derived based on the kinetic system (2.10).

3. Lattice Boltzmann model of mixture momentum and energy

3.1. *First law of thermodynamics for ideal gas mixture*

For further references and notation, we open this section with a summary of the first law of thermodynamics for ideal gas mixtures. Since non-reactive mixtures are considered in the following, the energy of formation is not included. The caloric equation of state of a single-component ideal gas provides for the specific mole-based sensible internal energy of species a:

$$\bar{U}_a = \int_{T_0}^{T} \bar{C}_{a,v}(T)\, \mathrm{d}T. \tag{3.1}$$

Here, $\bar{C}_{a,v}$ is the specific heat at constant volume. Thus, the sensible specific enthalpy reads as

$$\bar{H}_a = \int_{T_0}^{T} \bar{C}_{a,p}(T)\, \mathrm{d}T, \tag{3.2}$$

where $\bar{C}_{a,p}$ is the specific heat at constant pressure defined by Mayer's relation,

$$\bar{C}_{a,p} - \bar{C}_{a,v} = R_U. \tag{3.3}$$

Proceeding from the mole basis onto the mass basis, the specific heats are defined relative to the molar mass,

$$C_{a,v} = \frac{\bar{C}_{a,v}}{m_a}, \tag{3.4}$$

$$C_{a,p} = \frac{\bar{C}_{a,p}}{m_a}, \tag{3.5}$$

while the mass-based specific sensible internal energy and enthalpy are

$$U_a = \int_{T_0}^{T} C_{a,v}(T)\,\mathrm{d}T, \tag{3.6}$$

$$H_a = \int_{T_0}^{T} C_{a,p}(T)\,\mathrm{d}T. \tag{3.7}$$

Finally, the Mayer relation in the mass basis reads as

$$C_{a,p} - C_{a,v} = R_a, \tag{3.8}$$

where the gas constant R_a is defined by (2.9).

Switching to the case of a M-component mixture, the mixture internal energy ρU is defined on the mass basis as follows:

$$\rho U = \sum_{a=1}^{M} \rho_a U_a. \tag{3.9}$$

The specific mixture internal energy U can be rewritten as

$$U = \sum_{a=1}^{M} Y_a U_a = \sum_{a=1}^{M} Y_a \int_{T_0}^{T} C_{a,v}\,\mathrm{d}T = \int_{T_0}^{T} \left[\sum_{a=1}^{M} Y_a C_{a,v}\right] \mathrm{d}T = \int_{T_0}^{T} C_v\,\mathrm{d}T, \tag{3.10}$$

where the specific heat at constant volume is the mass-averaged value over the composition,

$$C_v = \sum_{a=1}^{M} Y_a C_{a,v}. \tag{3.11}$$

Similarly, the mixture enthalpy ρH is defined as

$$\rho H = \sum_{a=1}^{M} \rho_a H_a, \tag{3.12}$$

while the specific mixture enthalpy H can be transformed in the manner of (3.10),

$$H = \sum_{a=1}^{M} Y_a H_a = \sum_{a=1}^{M} Y_a \int_{T_0}^{T} C_{a,p}\,\mathrm{d}T = \int_{T_0}^{T} \left[\sum_{a=1}^{M} Y_a C_{a,p}\right] \mathrm{d}T = \int_{T_0}^{T} C_p\,\mathrm{d}T. \tag{3.13}$$

The specific heat at constant pressure reads as

$$C_p = \sum_{a=1}^{M} Y_a C_{a,p}, \tag{3.14}$$

while both the specific heats satisfy the Mayer relation,

$$C_p - C_v = R, \tag{3.15}$$

with the mixture gas constant R defined by (2.5). In the following, we formulate the lattice Boltzmann equation for the mixture density, momentum and energy for a generic case of temperature-dependent specific heats of the components.

3.2. *Two-population lattice Boltzmann equation for the mixture*

Point of departure is a lattice Boltzmann model for a single-component ideal gas with variable Prandtl number and adiabatic exponent. To that end, several suitable single-component lattice Boltzmann models exist in the literature; here we mention compressible LBM by Frapolli *et al.* (2015), Frapolli, Chikatamarla & Karlin (2016*a*) and Saadat *et al.* (2019). The common feature of these single-component models is the use of the double-population construction, the idea first introduced in the context of incompressible thermal convective LBM in the classical paper by He *et al.* (1998) and further expanded in Guo *et al.* (2007), Karlin, Sichau & Chikatamarla (2013), Frapolli, Chikatamarla & Karlin (2018). One set of populations, commonly quoted as f-populations, represents the density and momentum as the locally conserved fields of the corresponding f-LBM equation while another set, the g-populations, represents the energy as the local conservation of the g-LBM kinetics. The coupling between the f- and g-LBM equations is also well understood and enables the realization of an adjustable Prandtl number and adiabatic exponent. Various realizations differ by the choice of the discrete velocities of the f- and g-sets; in particular, the compressible LBM of Frapolli *et al.* (2015) employs higher-order lattices with higher isotropy while the two-dimensional model developed in Saadat *et al.* (2019) uses the standard lattice with correction terms to compensate for insufficient isotropy.

Whichever single-component double-population model is taken as the starting point for representing a multicomponent mixture, the central question is how to modify it. Note that, this question would not arise if one would follow the conventional approach by extending the already available M species LBM equations of § 2 to represent the energy equation of the mixture. However, with the double-population approach, this would lead to $2 \times M$ lattices since the lattice for each component would need to be doubled to represent the energy of that component. On the contrary, the mean-field approach pursuit here avoids the kinetic representation of partial energies, instead it addresses only the total energy of the mixture by a single g-set. This requires only $M + 2$ lattices, M for the species and two for the mixture momentum and energy.

In the following, we refer to the f-populations as the momentum lattice, and the g-populations as the energy lattice. For the momentum lattice, the locally conserved fields are the density and the momentum of the mixture,

$$\sum_{i=0}^{Q-1} f_i = \rho, \tag{3.16}$$

$$\sum_{i=0}^{Q-1} f_i \boldsymbol{c}_i = \rho \boldsymbol{u}. \tag{3.17}$$

For the energy lattice, the locally conserved field is the total energy of the mixture,

$$\sum_{i=0}^{Q-1} g_i = \rho E. \tag{3.18}$$

Here, the total energy ρE is the sum of the mixture internal energy ρU (3.10) and the kinetic energy $\rho u^2/2$,

$$\rho E = \rho U + \frac{\rho u^2}{2}. \tag{3.19}$$

Since the mixture internal energy (3.10) depends on the composition, it is the first instance where the species kinetic equations become coupled with the kinetic equations for the mixture. Conversely, the temperature of the mixture is computed from the integral equation,

$$\int_{T_0}^{T} C_v(T)\,\mathrm{d}T = E - \frac{u^2}{2}. \tag{3.20}$$

The temperature evaluated from solving (3.20) is used as the input in the definition of the pressure P in the equilibrium and quasi-equilibrium constraints of the species lattice Boltzmann system. This furnishes the input from the energy lattice into the species lattices.

We comment that, in the present section, the mixture density (3.16) and momentum (3.17) are defined self-consistently in the sense of f-populations of the momentum lattice. On the other hand, quantities carrying the same physical meaning were independently and also self-consistently defined earlier using the species populations, (2.59) and (2.58), respectively. Doubling of the conservation of the total mass and momentum is the feature of the intermediate steps of the construction during which the species subsystem and the mixture subsystem are set-up independently from one another. At the end of the construction, the doubling of the conservation shall be resolved through a coupling of both the species and the mixture subsystems in § 3.5.

The lattice Boltzmann equations for the momentum and for the energy lattice are patterned from the single-component developments,

$$f_i(\boldsymbol{x} + \boldsymbol{c}_i\delta t, t + \delta t) - f_i(\boldsymbol{x}, t) = \omega(f_i^{eq} - f_i), \tag{3.21}$$

$$g_i(\boldsymbol{x} + \boldsymbol{c}_i\delta t, t + \delta t) - g_i(\boldsymbol{x}, t) = \omega_1(g_i^{eq} - g_i) + (\omega - \omega_1)(g_i^{*} - g_i), \tag{3.22}$$

where relaxation parameters ω and ω_1 shall be related to the viscosity and thermal conductivity in the following. We now proceed with specifying the constraints on the equilibrium populations f_i^{eq} and g_i^{eq}, and the quasi-equilibrium g_i^{*} in order that the system (3.21) and (3.22) recovers the momentum and energy equations of the mixture.

First, the equilibrium populations must satisfy the $D + 2$ conservation laws,

$$\sum_{i=0}^{Q-1} f_i^{eq} = \rho, \tag{3.23}$$

$$\sum_{i=0}^{Q-1} f_i^{eq}\boldsymbol{c}_i = \rho\boldsymbol{u}, \tag{3.24}$$

$$\sum_{i=0}^{Q-1} g_i^{eq} = \rho E. \tag{3.25}$$

Second, the equilibrium pressure tensor $\boldsymbol{P}^{eq}$ and the tensor of equilibrium third-order moments $\boldsymbol{Q}^{eq}$ of the momentum lattice must verify the Maxwell–Boltzmann relations in order to recover the compressible flow momentum equation,

$$\boldsymbol{P}^{eq} = \sum_{i=0}^{Q-1} f_i^{eq}\boldsymbol{c}_i \otimes \boldsymbol{c}_i = P\boldsymbol{I} + \rho\boldsymbol{u} \otimes \boldsymbol{u}, \tag{3.26}$$

$$\boldsymbol{Q}^{eq} = \sum_{i=0}^{Q-1} f_i^{eq}\boldsymbol{c}_i \otimes \boldsymbol{c}_i \otimes \boldsymbol{c}_i = P\overline{\boldsymbol{u} \otimes \boldsymbol{I}} + \rho\boldsymbol{u} \otimes \boldsymbol{u} \otimes \boldsymbol{u}, \tag{3.27}$$

where the overline denotes symmetrization. Similarly, the equilibrium mixture energy flux $\boldsymbol{q}^{eq}$ and the second-order moment tensor $\boldsymbol{R}^{eq}$ pertinent to the energy lattice are

$$\boldsymbol{q}^{eq} = \sum_{i=0}^{Q-1} g_i^{eq} \boldsymbol{c}_i = \left(H + \frac{u^2}{2}\right) \rho \boldsymbol{u}, \tag{3.28}$$

$$\boldsymbol{R}^{eq} = \sum_{i=0}^{Q-1} g_i^{eq} \boldsymbol{c}_i \otimes \boldsymbol{c}_i = \left(H + \frac{u^2}{2}\right) \boldsymbol{P}^{eq} + P \boldsymbol{u} \otimes \boldsymbol{u}. \tag{3.29}$$

The mixture equation of state P (2.4), the mixture gas constant R (2.5) and the specific enthalpy of the mixture H (3.13) entering the constraints (3.26)–(3.28), (3.28) and (3.29) depend linearly on the composition through the local mass fractions Y_a.

To that end, the constraints on the equilibrium populations of the mixture momentum and energy lattices is a straightforward extension of those of the single-component double-population LBM for compressible flows where the ideal gas equation of state, the internal energy and the enthalpy are merely replaced by their mixture-averaged counterparts. A major difference comes next with the constraints for the quasi-equilibrium. The zeroth-, first- and second-order moments of the quasi-equilibrium populations g_i^*, or the quasi-equilibrium energy ρE^*, the energy flux $\boldsymbol{q}^*$ and the flux of the energy flux $\boldsymbol{R}^*$, respectively, have to satisfy the following relations:

$$\rho E^* = \sum_{i=0}^{Q-1} g_i^* = \rho E, \tag{3.30}$$

$$\boldsymbol{q}^* = \sum_{i=0}^{Q-1} g_i^* \boldsymbol{c}_i = \boldsymbol{q} - \boldsymbol{u} \cdot (\boldsymbol{P} - \boldsymbol{P}^{eq}) + \boldsymbol{q}^{diff} + \boldsymbol{q}^{corr}, \tag{3.31}$$

$$\boldsymbol{R}^* = \sum_{i=0}^{Q-1} g_i^* \boldsymbol{c}_i \otimes \boldsymbol{c}_i = \boldsymbol{R}^{eq}. \tag{3.32}$$

The first and third of these quasi-equilibrium constraints, (3.30) and (3.32), as well as the first and second terms in the quasi-equilibrium energy flux (3.31) are again the direct extension of the single-component LBM. Specifically, the two first terms in (3.31), comprising the energy flux $\boldsymbol{q}$ and the pressure tensor $\boldsymbol{P}$,

$$\boldsymbol{q} = \sum_{i=0}^{Q-1} g_i \boldsymbol{c}_i, \tag{3.33}$$

$$\boldsymbol{P} = \sum_{i=0}^{Q-1} f_i \boldsymbol{c}_i \otimes \boldsymbol{c}_i, \tag{3.34}$$

are needed to decouple the viscosity from thermal conductivity, and to maintain a variable Prandtl number, in both the single-component and multicomponent cases.

The remaining two terms in the quasi-equilibrium energy flux (3.31), $\boldsymbol{q}^{diff}$ and $\boldsymbol{q}^{corr}$, are specific to the multicomponent case and appear due to the mean-field approach to the

energy representation. The interdiffusion energy flux $\boldsymbol{q}^{diff}$ reads as

$$\boldsymbol{q}^{diff} = \left(\frac{\omega_1}{\omega - \omega_1}\right) \rho \sum_{a=1}^{M} H_a Y_a \boldsymbol{V}_a, \tag{3.35}$$

where the transformed diffusion velocities $\boldsymbol{V}_a$ are defined according to (2.55). The interdiffusion energy flux contributes the enthalpy transport due to diffusion and, hence, it vanishes in the single-component case. The effect of the interdiffusion energy flux is typically significant at the initial stages of the diffusion process and cannot be neglected.

Finally, the correction flux $\boldsymbol{q}^{corr}$ reads as

$$\boldsymbol{q}^{corr} = \frac{1}{2}\left(\frac{\omega_1 - 2}{\omega_1 - \omega}\right) \delta t P \sum_{a=1}^{M} H_a \nabla Y_a, \tag{3.36}$$

and is explained by the following consideration. The thermal flux is the mixture average of the component thermal fluxes, $\boldsymbol{q}^{th} = \sum_{a=1}^{M} Y_a \boldsymbol{q}_a^{th}$, where $\boldsymbol{q}_a^{th} = -\tau P C_{a,p} \nabla T$ is the Fourier law for the component, τ is a parameter of no importance to the current consideration. On the other hand, in the single-component LBM, the thermal flux is $\boldsymbol{q}_{sc}^{th} = -\tau P \nabla H_{sc}$, and with the single-component enthalpy H_{sc} it returns the Fourier law in this case. However, the extension of the single-component to the multicomponent case so far invokes only the replacement of the single-component enthalpy with the 'lumped' mixture enthalpy and without any correction one gets

$$\boldsymbol{q}^{lump} = -\tau P \nabla \left(\sum_{a=1}^{M} Y_a H_a\right) = \boldsymbol{q}^{th} - \tau P \sum_{a=1}^{M} H_a \nabla Y_a. \tag{3.37}$$

Thus, apart from the mixture-averaged Fourier law $\boldsymbol{q}^{th}$, the thermal flux also contains a spurious term. The spurious term is eliminated by the correction flux $\boldsymbol{q}^{corr}$ (3.36), where the prefactor is chosen by considering the hydrodynamic limit; see appendix B. The correction flux vanishes if all components are thermodynamically indistinguishable, that is, if all species have the same specific heat. In many cases, the correction flux contributes negligibly, for example, for air at moderate temperatures where the standard-air assumptions for diatomic molecules holds to a good approximation.

3.3. *Hydrodynamic limit of the two-population lattice Boltzmann model for mixtures*

Constraints on the pertinent equilibrium and quasi-equilibrium moments (3.26)–(3.31), (3.35), (3.36) and (3.32) are sufficient to study the hydrodynamic limit of the two-population lattice Boltzmann system (3.21) and (3.22) without a complete specification of the equilibrium and the quasi-equilibrium populations. The analysis follows the route of expanding the propagation to second order in the time step δt and evaluating the moments of the resulting expansion. Details of the derivation are included in appendix B, here we present the final result.

The continuity equation:

$$\partial_t \rho + \nabla \cdot (\rho \boldsymbol{u}) = 0. \tag{3.38}$$

The momentum equation:

$$\partial_t (\rho \boldsymbol{u}) + \nabla \cdot (\rho \boldsymbol{u} \otimes \boldsymbol{u}) + \nabla \cdot \boldsymbol{\pi} = 0. \tag{3.39}$$

Here, the pressure tensor $\boldsymbol{\pi}$ reads as

$$\boldsymbol{\pi} = P\boldsymbol{I} - \mu \left(\boldsymbol{S} - \frac{2}{D} (\nabla \cdot \boldsymbol{u}) \boldsymbol{I} \right) - \varsigma (\nabla \cdot \boldsymbol{u}) \boldsymbol{I}, \tag{3.40}$$

where $\boldsymbol{S}$ is the strain rate,

$$\boldsymbol{S} = \nabla \boldsymbol{u} + \nabla \boldsymbol{u}^{\dagger}. \tag{3.41}$$

The dynamic viscosity μ and the bulk viscosity ς are related to the relaxation parameter ω,

$$\mu = \left(\frac{1}{\omega} - \frac{1}{2} \right) P \delta t, \tag{3.42}$$

$$\varsigma = \left(\frac{1}{\omega} - \frac{1}{2} \right) \left(\frac{2}{D} - \frac{R}{C_v} \right) P \delta t. \tag{3.43}$$

The energy equation:

$$\partial_t (\rho E) + \nabla \cdot (\rho E \boldsymbol{u}) + \nabla \cdot \boldsymbol{q} + \nabla \cdot (\boldsymbol{\pi} \boldsymbol{u}) = 0. \tag{3.44}$$

Here, the heat flux $\boldsymbol{q}$ reads as

$$\boldsymbol{q} = -\lambda \nabla T + \rho \sum_{a=1}^{M} H_a Y_a V_a. \tag{3.45}$$

The first term is the Fourier law of thermal conduction, with thermal conductivity λ related to the relaxation parameter ω_1,

$$\lambda = \left(\frac{1}{\omega_1} - \frac{1}{2} \right) P C_p \delta t. \tag{3.46}$$

The second term in (3.45) is the interdiffusion energy flux. Some comments are in order.

(i) The continuity, the momentum and the energy equations are the standard equations for multicomponent compressible mixtures (Williams 1985; Bird *et al.* 2006).

(ii) The bulk viscosity vanishes if all components are monatomic, $\bar{C}_{a,v} = DR_U/2$.

(iii) Introducing the thermal diffusivity $\alpha = \lambda / \rho C_p$ and the kinematic viscosity $\nu = \mu / \rho$, the Prandtl number becomes

$$Pr = \frac{\nu}{\alpha} = \frac{\omega_1 (2 - \omega)}{\omega (2 - \omega_1)}. \tag{3.47}$$

(iv) Using the equation of state of the mixture (2.4) in (3.42) and (3.46), relaxation parameters ω and ω_1 are expressed in terms of dynamic viscosity and thermal conductivity,

$$\omega = \frac{2P\delta t}{P\delta t + 2\mu}, \tag{3.48}$$

$$\omega_1 = \frac{2PC_p\delta t}{PC_p\delta t + 2\lambda}. \tag{3.49}$$

Finally, the dynamic viscosity μ and the thermal conductivity λ of the mixture at any point is evaluated as a function of the local composition by using the methods described in Wilke (1950) and Mathur, Tondon & Saxena (1967), respectively:

$$\mu = \sum_{a=1}^{M} \frac{\mu_a X_a}{\sum_{b=1}^{M} \phi_{ab} X_b}. \tag{3.50}$$

Here μ_a are the dynamic viscosity of the components while the dimensionless factor ϕ_{ab} is given by

$$\phi_{ab} = \frac{\left[1 + \sqrt{\frac{\mu_a}{\mu_b}}\sqrt{\frac{m_b}{m_a}}\right]^2}{\sqrt{8}\sqrt{1 + \frac{m_a}{m_b}}}. \tag{3.51}$$

The thermal conductivity of the mixture λ is calculated from the thermal conductivity of the components λ_a,

$$\lambda = \frac{1}{2}\left(\sum_{a=1}^{M} X_a\lambda_a + \frac{1}{\sum_{a=1}^{M} \frac{X_a}{\lambda_a}}\right). \tag{3.52}$$

3.4. *Realization on the standard lattice*

3.4.1. *Equilibrium and quasi-equilibrium*

In order to finalize the construction of the lattice Boltzmann equations for the mixture, we need to specify the choice of the momentum and the energy lattices, and to provide the corresponding equilibrium and quasi-equilibrium populations. To that end, the single-component lattice Boltzmann models satisfying the moment constraints of § 3.2 are known in the literature. These employ higher-order lattices with a relatively large number of discrete velocities such as $D2Q49$ ($Q = 49$ in two dimensions, Frapolli *et al.* 2015) or $D3Q39$ ($Q = 39$ in three dimensions, Frapolli, Chikatamarla & Karlin 2020).

In this paper we develop the standard $D3Q27$ lattice realization as in the above case of the species LBM of § 2.4. We thus consider a two-dimensional compressible single-component lattice Boltzmann model by Saadat *et al.* (2019) on the standard $D2Q9$ velocity set. Since the $D2Q9$ and $D3Q27$ belong to the same family of product lattices,

cf. Karlin & Asinari (2010), it is natural to consider compressible LBM of Saadat *et al.* (2019) for our purpose. In the following, we extend the model of Saadat *et al.* (2019) to the three-dimensional $D3Q27$ discrete velocities set.

For the evaluation of the equilibrium g_i^{eq} and of the quasi-equilibrium g_i^* of the energy lattice, we proceed with the following ansatz $\mathcal{G}_i$, parameterized with a scalar $\theta \in [0, 1]$, a scalar M_0, a vector $\boldsymbol{m}$ and a second-order tensor $\boldsymbol{M}$,

$$\mathcal{G}_i(\theta, M_0, \boldsymbol{m}, \boldsymbol{M}) = h_i(\theta, M_0, \boldsymbol{m}, \boldsymbol{M}) + \boldsymbol{B}_i \cdot \boldsymbol{Z}(\theta, M_0, \boldsymbol{M}), \tag{3.53}$$

$$h_i(\theta, M_0, \boldsymbol{m}, \boldsymbol{M}) = w_i(\theta)\left(M_0 + \frac{\boldsymbol{m}\cdot\boldsymbol{c}_i}{\theta} + \frac{(\boldsymbol{M} - M_0\theta\boldsymbol{I}) : (\boldsymbol{c}_i\otimes\boldsymbol{c}_i - \theta\boldsymbol{I})}{2\theta^2}\right). \tag{3.54}$$

Here, the weights w_i are calculated in the product form as

$$w_i = w_{c_{ix}} w_{c_{iy}} w_{c_{iz}}, \tag{3.55}$$

based on the fundamental triplet,

$$w_0 = 1 - \theta, \quad w_1 = \frac{\theta}{2}, \quad w_{-1} = \frac{\theta}{2}. \tag{3.56a–c}$$

Furthermore, in (3.53), $\boldsymbol{Z}$ is a vector with the components

$$Z_\alpha = \frac{(1-3\theta)}{2\theta}(M_{\alpha\alpha} - \theta M_0). \tag{3.57}$$

Here, $M_{\alpha\alpha}$ is the diagonal component of the second-order tensor $\boldsymbol{M}$, while the components of vectors $\boldsymbol{B}_i$ are defined as follows:

$$\left.\begin{aligned} B_{i\alpha} &= 1 && \text{for } c_i^2 = 0,\\ B_{i\alpha} &= -\tfrac{1}{2}|c_{i\alpha}| && \text{for } c_i^2 = 1,\\ B_{i\alpha} &= 0 && \text{otherwise.}\end{aligned}\right\} \tag{3.58}$$

Note that, when the parameter θ is set to the lattice reference temperature $\theta = 1/3$, the term in (3.57) vanishes and the remaining term (3.54) becomes the familiar second-order Grad's approximation (Grad 1949). By construction, the form (3.53) satisfies the moment relations, for any θ:

$$\sum_{i=0}^{Q-1}\{1, \boldsymbol{c}_i, \boldsymbol{c}_i\otimes\boldsymbol{c}_i\}\mathcal{G}_i(\theta, M_0, \boldsymbol{m}, \boldsymbol{M}) = \{M_0, \boldsymbol{m}, \boldsymbol{M}\}. \tag{3.59}$$

The equilibrium and the quasi-equilibrium populations g_i^{eq} and g_i^* are defined with the help of the form (3.53) by specifying the parameters $\theta = RT$, $M_0 = \rho E$ and $\boldsymbol{M} = \boldsymbol{R}^{eq}$ (3.29) in both cases, and $\boldsymbol{m} = \boldsymbol{q}^{eq}$ (3.28) or $\boldsymbol{m} = \boldsymbol{q}^*$ (3.31) for the equilibrium or the quasi-equilibrium, respectively, following Saadat *et al.* (2019):

$$g_i^{eq} = \mathcal{G}_i(RT, \rho E, \boldsymbol{q}^{eq}, \boldsymbol{R}^{eq}), \tag{3.60}$$

$$g_i^{*} = \mathcal{G}_i(RT, \rho E, \boldsymbol{q}^{*}, \boldsymbol{R}^{eq}). \tag{3.61}$$

We shall now proceed with identifying the equilibrium of the momentum lattice and the modification of the lattice Boltzmann equation necessary for the $D3Q27$ model.

3.4.2. *Augmented lattice Boltzmann equation for the momentum lattice*

Equilibrium populations of the momentum lattice f_i^{eq} are evaluated in the conventional way with the help of the product form (2.34) and using $\boldsymbol{\xi} = \boldsymbol{u}$ and $\zeta = RT$,

$$f_i^{eq} = \rho \Psi_i(\boldsymbol{u}, RT). \tag{3.62}$$

It is well known that the diagonal element of the equilibrium third-order moment of the momentum lattice $Q_{\alpha\alpha\alpha}^{eq}$ cannot satisfy the required moment relation (3.27). This happens due to the lattice constraint, $c_{i\alpha}^3 = c_{i\alpha}$, which makes the diagonal third-order moments linearly dependent on the momentum, cf., e.g., Karlin & Asinari (2010). Following Saadat *et al.* (2019), we consider the augmented lattice Boltzmann equation on the momentum lattice as

$$f_i(\boldsymbol{x} + \boldsymbol{c}_i, t + 1) = f_i(\boldsymbol{x}, t) + \omega(f_i^{eq} - f_i) + \boldsymbol{A}_i \cdot \boldsymbol{X}, \tag{3.63}$$

where $\boldsymbol{X}$ is the vector with the components $\alpha = x, y, z$,

$$X_\alpha = -\partial_\alpha \left[\left(\frac{1}{\omega} - \frac{1}{2} \right) \delta t \partial_\alpha (\rho u_\alpha (1 - 3RT) - \rho u_\alpha^3) \right], \tag{3.64}$$

and where the components of vectors $\boldsymbol{A}_i$ are defined as

$$\left.\begin{aligned} A_{i\alpha} &= \tfrac{1}{2} c_{i\alpha} \quad \text{for } c_i^2 = 1, \\ A_{i\alpha} &= 0 \qquad \text{otherwise.} \end{aligned}\right\} \tag{3.65}$$

This completes the realization of the mixture momentum and energy lattice Boltzmann equations on the standard $D3Q27$ lattice. In the next section we shall specify the coupling between the species and the mixture lattice Boltzmann subsystems.

3.5. *Weak and strong coupling*

3.5.1. *Weak coupling*

Summarizing, the lattice Boltzmann model for a compressible M-component mixture of ideal gas on the standard $D3Q27$ lattice consists of M species lattices where the lattice Boltzmann equation is given by (2.53), and the momentum and energy lattice Boltzmann equations (3.63) and (3.22). In total, the $M + 2$ lattice Boltzmann equations are tightly coupled. As has been already specified above, the temperature from the energy lattice is provided to the species lattices through species equilibrium (2.35) and quasi-equilibrium (2.36), but also in the Stefan–Maxwell temperature-dependent relaxation rates (2.31). On the other hand, the mass fractions from the species lattices are used to compute the mixture energy and enthalpy in the equilibrium and the quasi-equilibrium of the momentum and energy lattices. Another coupling is the input of species diffusion velocities into the quasi-equilibrium population of the energy lattice via the interdiffusion flux (3.35). Finally, the momentum and the energy lattices are coupled in the standard way already present in the single-component setting. This entire set of interconnections between the species, and the momentum and energy lattices shall be termed the weak coupling.

3.5.2. *Strong coupling: Matching of mixture density and momentum*

With the two subsystems, the species and the mixture, first constructed independently from each other and after that being coupled weakly in the way described previously, we are left with two independent definitions of the mixture density and the

mixture momentum. On the one hand, the mixture density ρ (3.16) and the mixture momentum $\rho\boldsymbol{u}$ (3.17) are defined as the moments of the populations f_i. On the other hand, the same quantities are defined with the species populations as the sum of partial densities and partial momenta. The number of the conservation laws for the species subsystem is $M + D$, while for the mixture subsystem it is $D + 2$. The total number of the conservation laws in the weakly coupled combined system is $M + 2D + 2$. Thus, the weakly coupled system is in excess of $D + 1$ conservation laws as compared with the $M + D + 1$ conservation laws of the mixture. This redundancy can be eliminated by removing one set of species populations (here, the Mth) and writing

$$f_{Mi} = f_i - \sum_{a=1}^{M-1} f_{ai}. \tag{3.66}$$

As a consequence, the Mth component is not an independent field anymore but is slaved to the remaining species and mixture populations.

While this is the method of choice to avoid over-determination of the system, various other, weaker coupling strategies exist. For example, considering the mixture density and mixture momentum defined by the momentum lattice as primary, the excess in conservation laws can be resolved by replacing the density of a selected component ρ_M by the deficit of density once the $M - 1$ other components are taken into account. Similarly, the momentum of the Mth component $\rho_M\boldsymbol{u}_M$ accounts for the deficit of the mixture momentum once the momenta of the other species are counted,

$$\rho_M = \rho - \sum_{a=1}^{M-1} \rho_a = \sum_{i=1}^{Q-1} f_i - \sum_{a=1}^{M-1}\sum_{i=1}^{Q-1} f_{ai}, \tag{3.67}$$

$$\rho_M\boldsymbol{u}_M = \rho\boldsymbol{u} - \sum_{a=1}^{M-1} \rho_a\boldsymbol{u}_a = \sum_{i=1}^{Q-1} f_i\boldsymbol{c}_i - \sum_{a=1}^{M-1}\sum_{i=1}^{Q-1} f_{ai}\boldsymbol{c}_i. \tag{3.68}$$

In other words, only the density and momentum of the Mth component are slaved by the corresponding mixture quantities and the rest of the mixture composition. Hence, the lattice Boltzmann equation for the Mth component becomes purely relaxational, stripped of its conservation law. At the same time, the total momentum conservation is slaved by the momentum conservation of the momentum lattice. Since the relation (3.66) also implies (3.67) and (3.68), the number of independent conservation laws in both versions of the strongly coupled system is thus

$$(D + 2) + [(M + D) - 1 - D] = M + D + 1, \tag{3.69}$$

and corresponds to the locally conserved fields, $\rho_1, \ldots, \rho_{M-1}$, ρ, $\rho\boldsymbol{u}$ and ρE. While the assignment of the slaved component M is not unique, it is advisable to select the component which carries the majority of mass in the mixture.

In practice all couplings, the weak or the strong versions, yield identical results but the strongest coupling as in (3.66) is recommended as it reduces the number of lattices from $M + 2$ in other coupling strategies to $M + 1$.

4. Results

4.1. *Overview of numerical implementation*

In order to validate various physical aspects of the proposed lattice Boltzmann model, we consider four benchmarks as follows.

(i) Diffusion in a ternary gas mixture. This test case validates the Stefan–Maxwell diffusion and exhibits effects such as a diffusion barrier and uphill diffusion, which cannot be captured by Fick's diffusion assumption.
(ii) Diffusion in opposed jets. Here, we verify the coupling between the hydrodynamics and the diffusion model.
(iii) Speed of sound measurement in a mixture. This test case further validates the compressible model.
(iv) Three-dimensional Kelvin–Helmholtz instability. Finally, this canonical benchmark demonstrates the extension of the fully coupled model to three dimensions and, therefore, shows viability for complex flows including turbulence.

Thermodynamic data necessary for the simulations such as the specific heats, molecular masses and transport coefficients including dynamic viscosity, thermal conductivity and the Stefan–Maxwell diffusivities were obtained from the publicly accessible GRI-Mech 3.0 mechanism (Smith *et al.* 1999). The lattice Boltzmann code was coupled to the open source code Cantera (Goodwin *et al.* 2018) which is capable of parsing the GRI-Mech mechanism data file. The data required by the lattice Boltzmann solver during runtime is obtained by querying Cantera through its C++ API involving the 'IdealGasMix' and 'Transport' classes. The temperature was derived from the energy data output by solving (3.20) in the external loop by iteration. In all cases, we set the reference temperature $T_0 = 237.15$ K in (3.6). All data necessary for reproducing the test cases in this work is provided in appendix C for the interested reader to avoid using Cantera. The speed of sound c_s is defined as

$$c_s = \sqrt{\gamma RT}, \tag{4.1}$$

where both the adiabatic exponent $\gamma = C_p/C_v$ and the specific gas constant R depend on the mixture composition. In what follows, we use the acoustic scaling: The speed of sound (4.1) at a specified reference composition (typically, at the equilibrium) and specified temperature is used to make velocity non-dimensional, unless otherwise stated. The characteristic length is given in the respective set-up. Acoustic scaling was used to convert from physical to lattice units. Finally, the second-order accurate isotropic lattice operators proposed by Thampi *et al.* (2013) were used for the evaluation of spatial derivatives in the correction to the heat flux (3.36) as well as in the isotropy correction (3.64).

4.2. *Diffusion in a ternary gas mixture*

A classical experiment on diffusion in a ternary mixture of hydrogen H_2, argon Ar and methane CH_4 in a Loschmidt tube apparatus was performed by Arnold & Toor (1967); results of the experiment of Arnold & Toor (1967) were later analysed in depth by Krishna & Wesselingh (1997). The experiment of Arnold & Toor (1967) highlighted a number of, in part counter-intuitive, features of the Stefan–Maxwell diffusion. It is therefore natural to test our mixture model against the experiment of Arnold & Toor (1967).

The strongly coupled version of the three-dimensional lattice Boltzmann model for Stefan–Maxwell diffusion was realized on a quasi-one-dimensional domain with $864 \times 1 \times 1$ grid points. In order to represent a closed tube, the bounce-back boundary condition was used for all populations at each end of the tube, while periodic boundary conditions were applied in the other two directions. The same initial composition of the mixture as in the experiment of Arnold & Toor (1967) was used; the set-up was initialized with a uniform atmospheric pressure and temperature $T = 300$ K. It should be stressed that the temperature was not stipulated to be fixed during the simulation. Rather, the fully coupled

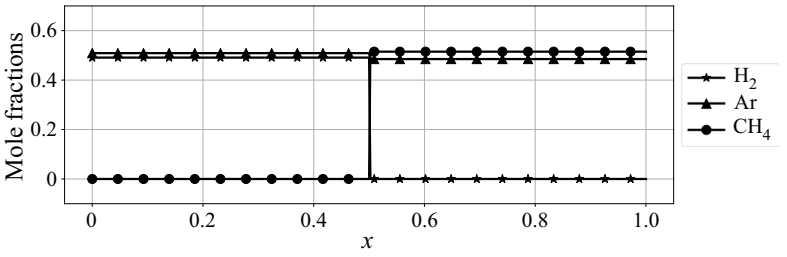

FIGURE 1. Diffusion in a ternary mixture, case 1*T* (Arnold & Toor 1967). Mole fractions of hydrogen H_2, argon Ar and methane CH_4 along the length of the tube as described by the initial conditions of (4.2).

thermo-hydrodynamic system maintained the isobaric and isothermal conditions by the initial and boundary conditions. As in the experiment, the evolution of the composition was represented by the average mole fraction of each species in the left and in the right halves of the tube. The non-dimensional time was used to represent the data, $t_{ND} = t/t_s$, where t_s is the time required for the sound wave to traverse the domain in a reference equilibrium composition.

In our first numerical experiment, the mole fractions of the species in the left and right halves of the tube were initiated as in the case 1*T* of Arnold & Toor (1967), see figure 1:

$$\left.\begin{aligned} \text{Left:}\quad & X_{\mathrm{H_2}} = 0.491, X_{\mathrm{Ar}} = 0.509, X_{\mathrm{CH_4}} = 0.000, \\ \text{Right:}\quad & X_{\mathrm{H_2}} = 0.000, X_{\mathrm{Ar}} = 0.485, X_{\mathrm{CH_4}} = 0.515. \end{aligned}\right\} \tag{4.2}$$

Time evolution of hydrogen H_2 and methane CH_4 follows Fick's diffusion law: the species from the higher concentration side reduce in mole fractions as they move towards the low concentration side. Thus, CH_4 can be seen moving from right to left and H_2 in the opposite direction, both species eventually attaining a uniform concentration.

However, the behaviour of argon Ar cannot be explained by Fick's law. Although Ar has a negligible concentration gradient due to the initial conditions (4.2), it does start diffusing, see figure 2. This phenomenon was termed osmotic diffusion by Toor (1957). Osmotic diffusion is said to occur when the rate of diffusion of a component is not zero even though its concentration gradient is negligible; this would correspond to an infinite Fick's diffusivity. The concentration of Ar keeps on growing in the left section even though its concentration is higher in the left section itself, see figure 2. The effect was termed uphill diffusion (or reverse diffusion) in Toor (1957) because the component diffuses in the direction of increase of its concentration; in Fick's picture this would amount to negative diffusivity. The reverse diffusion is seen to proceed for some time and then flattens at $t_{ND} \approx 400$. At this point in time, an appreciable concentration gradient is built up but the diffusion is negligible, see figure 3. The effect was termed a diffusion barrier in Krishna & Wesselingh (1997), the point at which the diffusion rate of a component vanishes even though its concentration gradient does not. This would mean zero Fick's diffusivity. After the diffusion barrier, the ordinary Fick's diffusion sets in and proceeds downhill of the concentration gradient until the uniform steady state is reached, see figures 4 and 5.

Figure 6 shows the evolution of the average mole fractions of the species in the left and right halves of the tube. The effects just mentioned were observed in the experiment of Arnold & Toor (1967) and in an earlier similar experiment by Duncan & Toor (1962). Krishna & Wesselingh (1997) provided an explanation by drawing an analogy between the

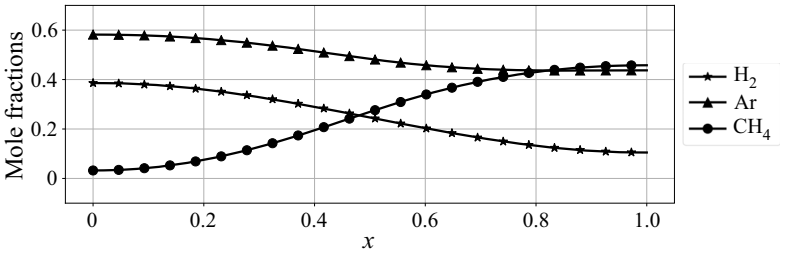

FIGURE 2. Case 1*T*. Mole fractions of hydrogen H_2, argon Ar and methane CH_4 along the length of the tube during uphill diffusion of Ar at $t_{ND} = 179.52$.

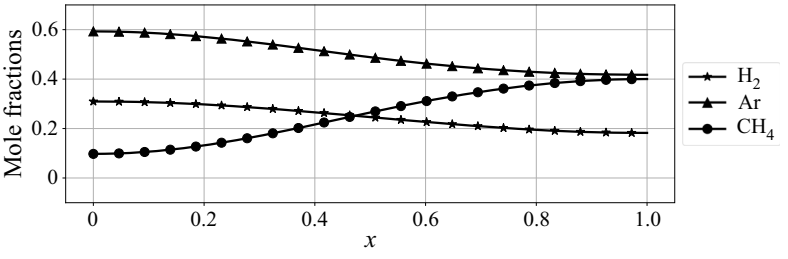

FIGURE 3. Case 1*T*. Mole fractions of hydrogen H_2, argon Ar and methane CH_4 along the length of the tube at the diffusion barrier, $t_{ND} = 378.98$.

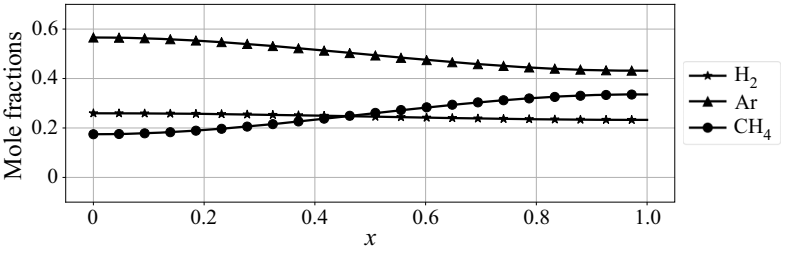

FIGURE 4. Case 1*T*. Mole fractions of hydrogen H_2, argon Ar and methane CH_4 along the length of the tube during Fickian diffusion of argon after the diffusion barrier, $t_{ND} = 777.91$.

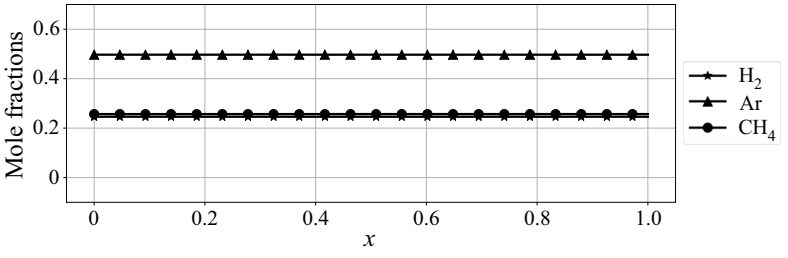

FIGURE 5. Case 1*T*. Mole fractions of hydrogen H_2, argon Ar and methane CH_4 along the length of the tube at the steady state, $t_{ND} = 6323.09$.

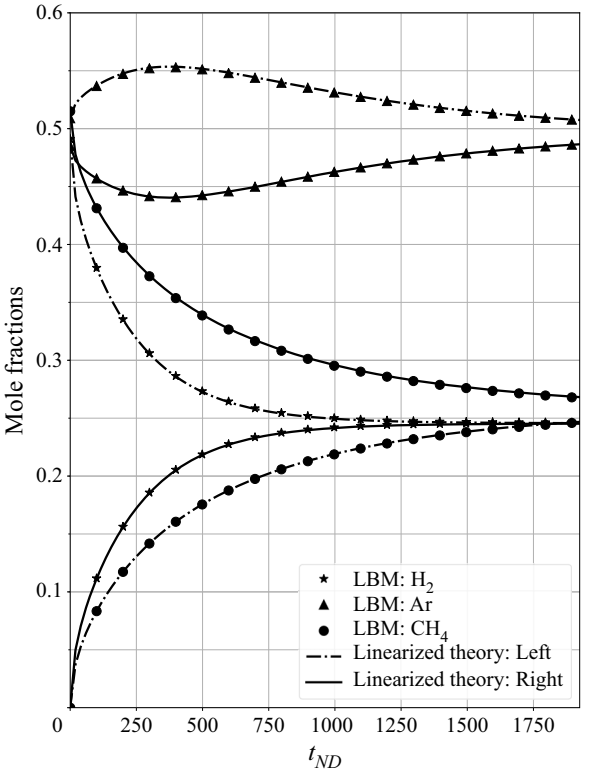

FIGURE 6. Diffusion in a ternary mixture, case 1*T* (Arnold & Toor 1967), (4.2). Averaged mole fractions of hydrogen H_2, argon Ar and methane CH_4 in the left and right halves of the tube. The figure shows reverse diffusion of argon. Symbol: present simulation; line: theory (Arnold & Toor 1967).

frictional drag and binary diffusion coefficients of pairs of species. According to Krishna & Wesselingh (1997), the Stefan–Maxwell diffusivity plays a role of an inverse drag coefficient. The binary diffusion coefficient between Ar and H_2 is 8.14543×10^{-5} m^2 s^{-1}, while that between Ar and CH_4 is 2.17321×10^{-5} m^2 s^{-1}. This means that the frictional drag exerted on Ar by CH_4 is much greater than that exerted on Ar by H_2. Thus, CH_4 drags Ar along with it during the initial period when the flux of CH_4 from right to left is large, causing the uphill diffusion of Ar. The transport of CH_4 from right to left eventually reduces because the driving force causing it reduces due to the reduction in concentration gradient of CH_4. At the same time, the increasing concentration of Ar creates a driving force for Ar to diffuse downhill. A balance is reached at the point of diffusion barrier after which the drag force caused by CH_4 is overcome and Ar starts diffusing downhill of its concentration in a Fick's fashion.

It is apparent from figure 6 that the lattice Boltzmann simulation was able to correctly capture the experimentally observed phenomena. For a more quantitative assessment, we compare simulation results with the linearized theory of multicomponent mass transfer proposed in Arnold & Toor (1967). The theory relies upon a semi-analytical solution of the one-dimensional diffusion equations for the average mole fractions using linearized Stefan–Maxwell relation for the diffusion fluxes, and was shown to match the experiment in a quantitative fashion (Arnold & Toor 1967). For the purpose of this study, we

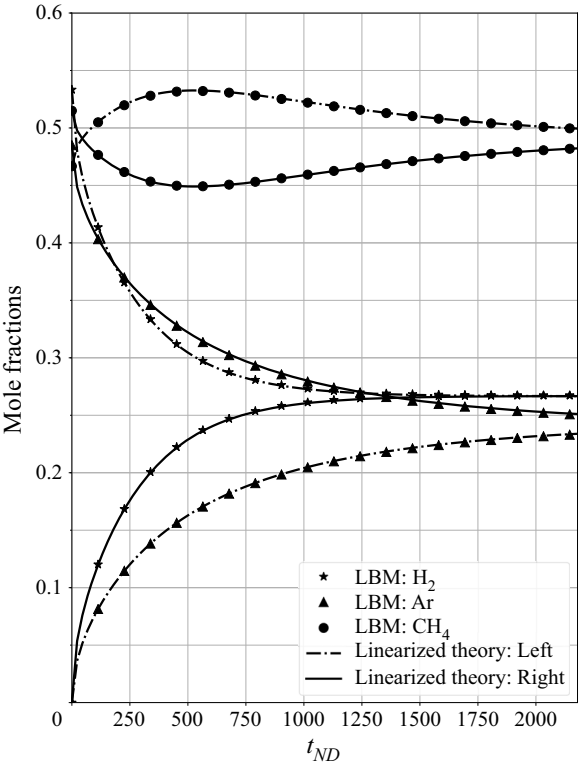

FIGURE 7. Diffusion in a ternary mixture, case 2T (Arnold & Toor 1967), (4.3). Averaged mole fractions of hydrogen H_2, argon Ar and methane CH_4 in the left and right halves of the tube. The figure shows reverse diffusion of methane. Symbol: present simulation; line: theory (Arnold & Toor 1967).

numerically solved the equations of the linearized theory using Python. As is evident from figure 6, the results of the simulation agree well with the linearized theory, both in terms of magnitudes of the mole fractions as well as the time.

Continuing along the lines of the experimental study, the simulation was repeated with a different set of initial conditions, corresponding to the case 2T of Arnold & Toor (1967):

$$\left.\begin{aligned} \text{Left:}\quad & X_{\mathrm{H_2}} = 0.512, X_{\mathrm{Ar}} = 0.000, X_{\mathrm{CH_4}} = 0.448, \\ \text{Right:}\quad & X_{\mathrm{H_2}} = 0.000, X_{\mathrm{Ar}} = 0.485, X_{\mathrm{CH_4}} = 0.515. \end{aligned}\right\} \tag{4.3}$$

According to the theory of the inverse relation between mass diffusivity and drag (Krishna & Wesselingh 1997), methane should now exhibit uphill diffusion due to the flux of argon. This is indeed what was seen in the experiments of Arnold & Toor (1967) as well as in our simulations, see figure 7. Simulations are in good agreement with the linearized theory.

A final but equally important situation is the one marked as case 3T in the experiment (Arnold & Toor 1967):

$$\left.\begin{aligned} \text{Left:}\quad & X_{\mathrm{H_2}} = 0.512, X_{\mathrm{Ar}} = 0.000, X_{\mathrm{CH_4}} = 0.448, \\ \text{Right:}\quad & X_{\mathrm{H_2}} = 0.491, X_{\mathrm{Ar}} = 0.509, X_{\mathrm{CH_4}} = 0.000. \end{aligned}\right\} \tag{4.4}$$

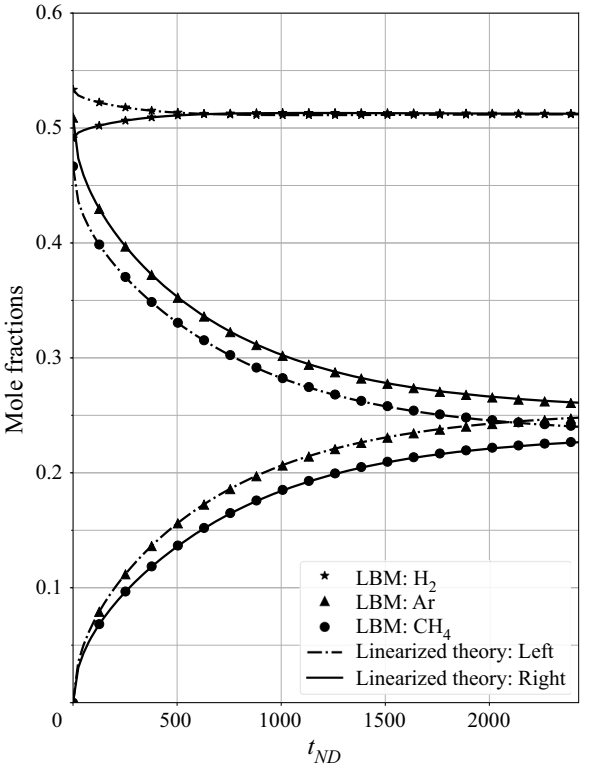

FIGURE 8. Diffusion in a ternary mixture, case 3*T* (Arnold & Toor 1967), (4.4). Averaged mole fractions of hydrogen H_2, argon Ar and methane CH_4 in the left and right halves of the tube. The figure shows near-Fickian diffusion of hydrogen. Symbol: present simulation; line: theory (Arnold & Toor 1967).

The binary diffusivity between Ar and H_2 is 8.14543×10^{-5} m^2 s^{-1}, while that between CH_4 and H_2 is 7.37433×10^{-5} m^2 s^{-1}. The diffusivities are comparable and, thus, the interaction of H_2 with Ar is very similar to the interaction of H_2 with CH_4. In figure 8 the results from the lattice Boltzmann simulation as well as the linearized theory show a nearly Fickian diffusion of H_2. Hydrogen however does show a small but nevertheless clear tendency to accumulate in the right half of the tube. This is possibly due to a slightly greater drag exerted on H_2 by CH_4 thanks to a somewhat smaller diffusivity between the pair.

For an additional validation, we compare the composition map of the simulation with the composition map of the experiment, since the composition map for the Stefan–Maxwell diffusion is independent of time (Duncan & Toor 1962). Figure 9 verifies that the composition paths of the simulations agree well with that of all the three experiments of Arnold & Toor (1967). The composition path that would be followed by a purely Fickian diffusion is also marked in figure 9 as 'Path w/o reverse diffusion' for the purpose of contrast. The set-ups eventually attain a homogeneous composition at the 'Equilibrium' points on the composition map located midway of the Fickian lines, at the intersection with the Stefan–Maxwell trajectory. It can be again seen in the composition map that even for the case 3*T*, the diffusion path of hydrogen is almost yet not purely Fickian.

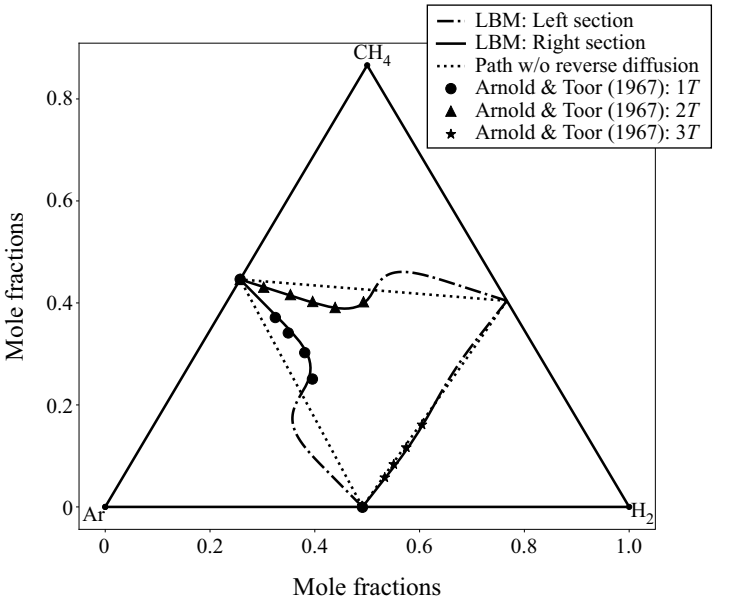

FIGURE 9. Composition path of the averaged mole fractions of H_2, Ar and CH_4 in the left and right halves of the tube. The composition path shows three different cases, each with a reverse diffusion of Ar, CH_4 and a nearly Fickian diffusion of hydrogen. Lines: present simulation; symbol: experiment of Arnold & Toor (1967).

4.3. *Diffusion in opposed jets*

In order to assess the coupling between the diffusion and the hydrodynamic systems we consider the case of planar opposed jets. The set-up and boundary conditions are similar to that studied in Arcidiacono *et al.* (2007). It consists of two facing jets of fluid with equal momentum and different compositions. As shown in figure 10, the simulation is performed on a grid of size $L_x \times L_y \times L_z = 200 \times 400 \times 1$ points, with the distance between the nozzles $L_x = 200$. For the inlets, the incoming populations are replaced by the equilibrium distributions while the outlets are modelled by making the derivative normal to the boundary zero. For the solid vertical boundaries at $y < 0.1L_y$ and $y > 0.9L_y$, a free-slip boundary condition is used. The compositions of the jet streams are

$$\left.\begin{aligned} \text{Left:}\quad & X_{\mathrm{H_2}} = 0.1, X_{\mathrm{N_2}} = 0.85, X_{\mathrm{O_2}} = 0.0, X_{\mathrm{H_2O}} = 0.05, \\ \text{Right:}\quad & X_{\mathrm{H_2}} = 0.0, X_{\mathrm{N_2}} = 0.90, X_{\mathrm{O_2}} = 0.1, X_{\mathrm{H_2O}} = 0.00. \end{aligned}\right\} \tag{4.5}$$

The solution of the present model at steady state is compared with the solution produced by the 'CounterflowDiffusionFlame' function of the open source package Cantera (Goodwin *et al.* 2018). This function computes a steady-state solution to counterflow diffusion flame using a reduced one-dimensional similarity solution, as derived in § 6.2 of Kee *et al.* (2003). In order to get a solution comparable with the Stefan–Maxwell formulation of the lattice Boltzmann model, the reactions are turned off in Cantera and the transport model is set to 'Multi', which accounts for the pairwise diffusion between the species. As can be seen in figure 11, the LBM solution for the mole fractions of all the components as well as the scaled velocity agree well with the solution produced by Cantera. It should be noted that this test case is regarded severe in Arcidiacono *et al.* (2007) since the diffusion

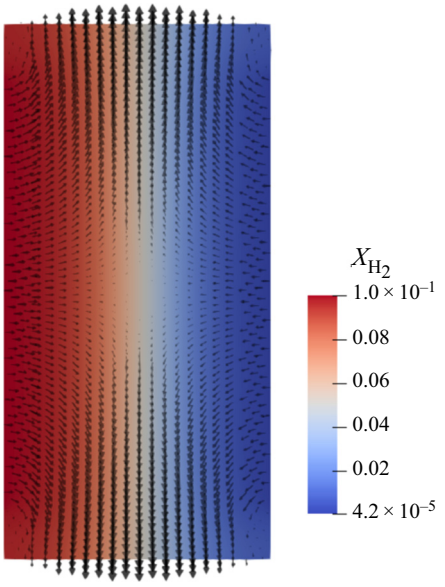

FIGURE 10. Contour of the mole fraction of H_2 and vectors of velocity at steady state for the opposed jets set-up. The velocity vectors are scaled by the magnitude of the velocity.

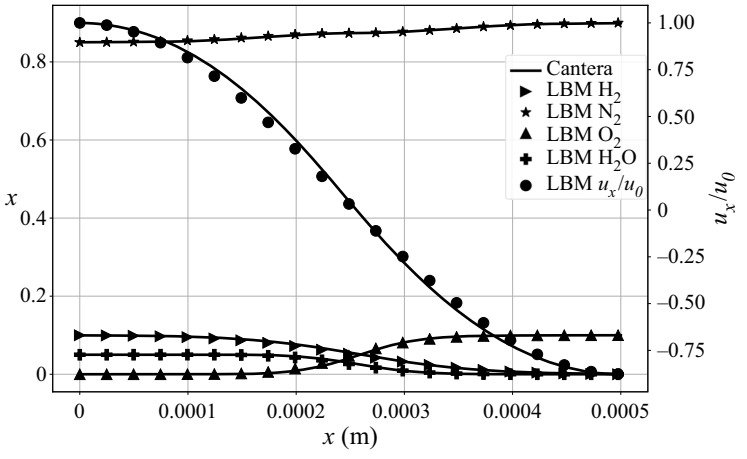

FIGURE 11. Mole fractions of H_2, N_2, O_2 and H_2O and flow velocity at stagnation line.

of the components proceeds against the velocity of the bulk flow. For example, hydrogen and water from the left nozzle diffuse against the bulk flow on the right side, upstream towards the right nozzle. The good agreement of the results indicates that the coupling of the Navier–Stokes and the Stefan–Maxwell models is consistent and correct.

4.4. *Speed of sound*

As a standard test for a compressible flow LBM, we verify that the model correctly reproduces the speed of sound c_s (4.1). The speed of sound was measured for the following

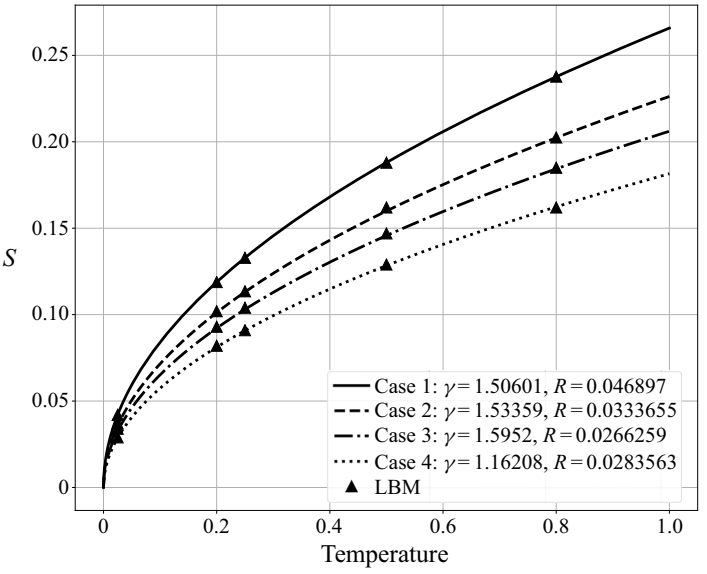

FIGURE 12. Speed of sound for different compositions (4.6). Symbol: simulation; line: theory, (4.1).

four compositions $S1$–$S4$:

$$\left.\begin{array}{ll}
(S1)\ R = 0.046897 & X_{H_2} = 0.491,\ X_{Ar} = 0.509,\ X_{CH_4} = 0.000,\\
(S2)\ R = 0.0333655 & X_{H_2} = 0.200,\ X_{Ar} = 0.700,\ X_{CH_4} = 0.100,\\
(S3)\ R = 0.026625 & X_{H_2} = 0.000,\ X_{Ar} = 0.900,\ X_{CH_4} = 0.100,\\
(S4)\ R = 0.0283563 & X_{H_2} = 0.200,\ X_{Ar} = 0.100,\ X_{C_3H_8} = 0.700.
\end{array}\right\} \tag{4.6}$$

Composition S1 in (4.6) is chosen from one of the cases in § 4.2, whereas the case S3 is chosen arbitrarily in order to test for the sound speed in a composition with a considerable difference in mole fractions. The cases S2 and S4 are chosen to verify the speed of sound in a ternary mixture and in the presence of heavier gases such as propane, respectively. The test is performed by tracking a small perturbation in pressure $\Delta P = 10^{-5}$ at a specified temperature T. Figure 12 compares the measured speed of the propagation of the perturbation with the theoretical speed of sound prediction (4.1). The lattice Boltzmann model correctly recovered the sound speed over a tested range of temperatures from $T_{min} = 0.025$ to $T_{max} = 0.8$ in lattice units. The tested temperature range is characterized by the ratio of the temperatures, $T_{max}/T_{min} = 32$, which is sufficiently large for many applications. Temperature between $T = 0.2$ to $T = 0.5$ in lattice units was used for most of the simulations presented in this paper.

4.5. *Kelvin–Helmholtz instability*

Without a pretence of an in-depth study of shear layer instabilities in this paper, the final example presents a three-dimensional simulation of the classical Kelvin–Helmholtz instability in order to validate the proposed model towards its possible use for high-Reynolds-number simulations. Similar to the set-up in San & Maulik (2018), we simulate the Kelvin-Helmholtz instability in a periodic domain of the size

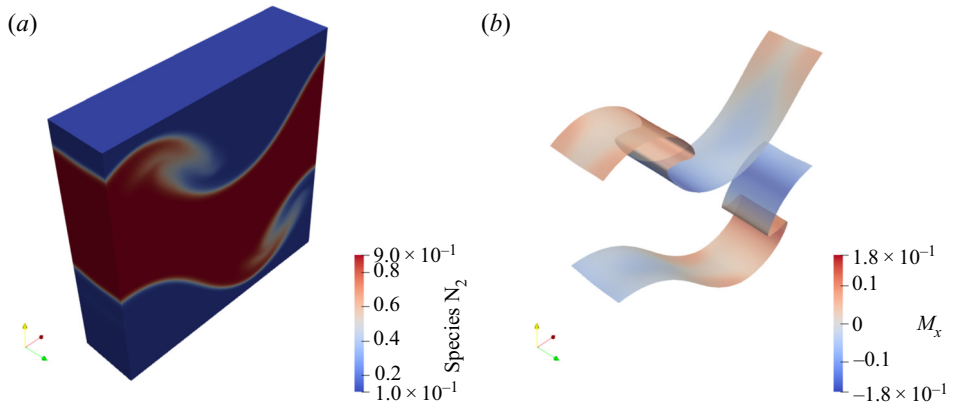

FIGURE 13. Contour of the mole fraction of nitrogen N_2 (a) and isosurface of the equilibrium concentration of nitrogen $X_{N_2} = 0.5$ coloured with the Mach number in the x-direction (b) at time $t_e = 2.2521$.

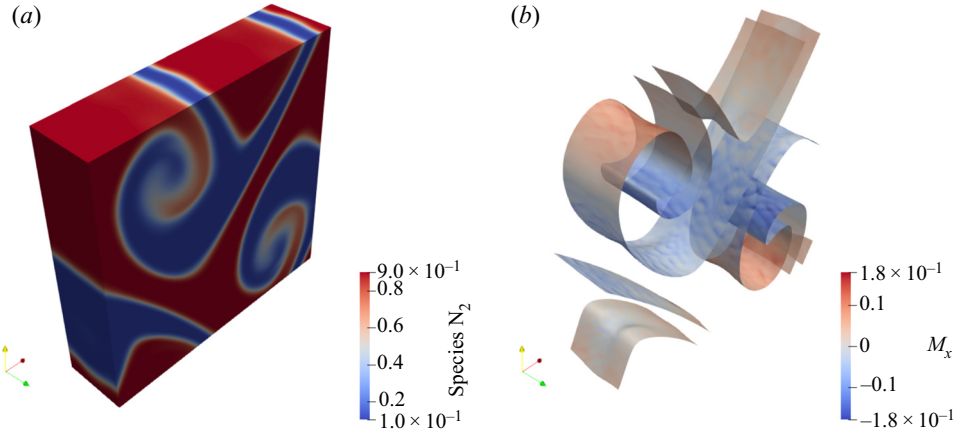

FIGURE 14. Contour of the mole fraction of nitrogen N_2 (a) and isosurface of the equilibrium concentration of nitrogen $X_{N_2} = 0.5$ coloured with the Mach number in the x-direction (b) at time $t_e = 3.3119$.

$L_x \times L_y \times L_z = 800 \times 800 \times 200$ lattice grid points. The domain is split into three sections in the flow-normal direction, where the initial conditions for a two-component mixture of nitrogen N_2 and water vapour H_2O are as follows:

$$\left.\begin{aligned} u_x &= 0.1M_c, \quad X_{H_2O} = 0.9, \quad X_{N_2} = 0.1, \quad \text{for } 0 \le y < 0.25L_y, \\ u_x &= -0.1M_c, \quad X_{H_2O} = 0.1, \quad X_{N_2} = 0.9, \quad \text{for } 0.25L_y \le y < 0.75L_y, \\ u_x &= 0.1M_c, \quad X_{H_2O} = 0.9, \quad X_{N_2} = 0.1, \quad \text{for } 0.75L_y \le y \le L_y. \end{aligned}\right\} \tag{4.7}$$

The velocity in the normal direction u_y and in the spanwise direction u_z is given by, respectively,

$$u_y = 2|u_x|0.01 \sin(2\pi x/L_x), \tag{4.8}$$

$$u_z = 2|u_x|0.01 \sin(2\pi z/L_z). \tag{4.9}$$

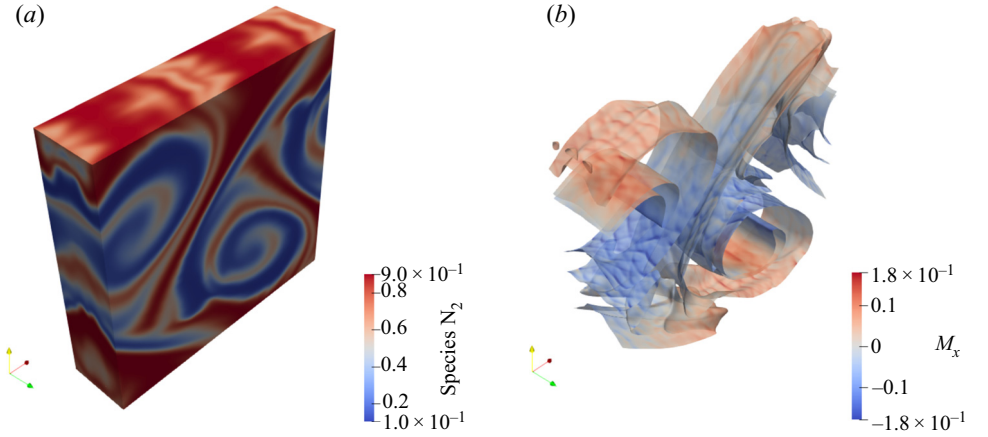

FIGURE 15. Contour of the mole fraction of nitrogen N_2 (*a*) and isosurface of the equilibrium concentration of nitrogen $X_{N_2} = 0.5$ coloured with the Mach number in the x-direction (*b*) at time $t_e = 4.901612$.

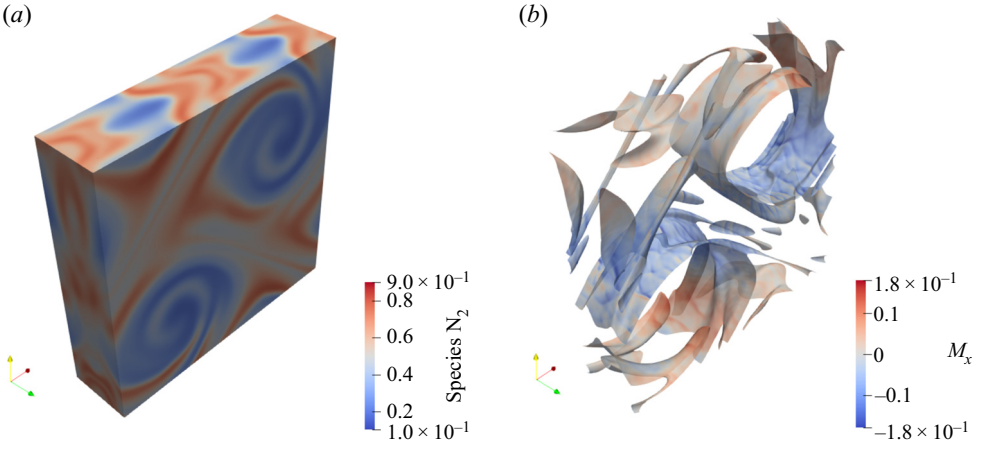

FIGURE 16. Contour of the mole fraction of nitrogen N_2 (*a*) and isosurface of the equilibrium concentration of nitrogen $X_{N_2} = 0.5$ coloured with the Mach number in the x-direction (*b*) at time $t_e = 8.345988$.

The initial composition of the binary mixture (4.7) is so chosen as to equilibrate at the 50/50 equilibrium composition $X_{N_2} = X_{H_2O} = 0.5$ in the absence of any flow. The initial condition (4.8) and (4.9) further introduces a small perturbation in both the normal and spanwise directions with a wavelength equal to the length of the domain and a magnitude of one percent of the relative shear velocity. As defined by Leep, Dutton & Burr (1993), the convective Mach number M_c is the Mach number relative to the frame of reference of the simulation. The relative Mach number M_r based on the relative velocity across the shear layers is $M_r = 0.2$ according to the initial conditions (4.7). The Reynolds number with respect to the viscosity of the bottom-most layer, with M_r as the velocity scale and L_y as the length scale is $Re = 11963.46$. The mole fractions are chosen as 0.1 and 0.9 to make the test more severe. We define an eddy turnover time $t_e = L_x/U_r$, with the initial relative velocity $U_r = 2|u_x|$.

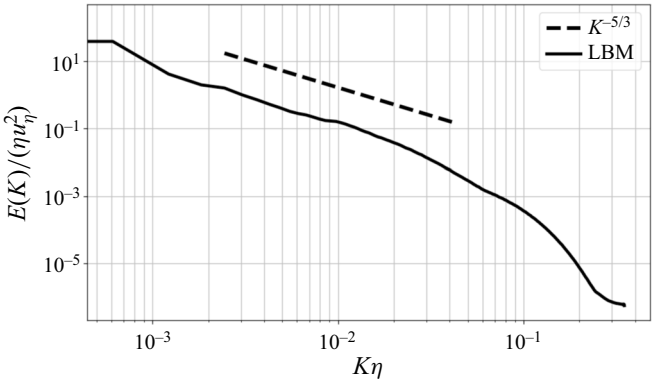

FIGURE 17. Turbulent kinetic energy spectrum at $t_e = 7.9486$ along with the theoretical Kolmogorov scaling. Here η is the Kolmogorov length scale and u_η is the Kolmogorov velocity.

We present contours and isosurfaces of the equilibrium mole fraction of nitrogen $X_{N_2} = 0.5$ at different times in figures 13–16. The isosurfaces are coloured by the x-component of the convective Mach number M_c to provide a visual indication of the direction of motion. Soon after the initial condition, the normal perturbation breaks the symmetry of the flow and the shear layer begins to curl up into a vortex without a significant spanwise deformation. This is evident in figure 13, where the three dimensionality of the flow is visible only in the non-uniform spanwise velocity of the isosurface. As the simulation proceeds, the flow in figure 14 develops anti-symmetric vortices which are also visibly deformed in the spanwise direction. This process continues and the vortices stretch and deform over time, which is visible in both the contours of the mole fraction of N_2 as well as the isosurfaces in figure 15. The flow eventually becomes more chaotic, forming smaller-scale structures in figure 16. It should not be forgotten that the components are also undergoing diffusion during this mixing, as evident from the smearing of the contour values over time.

While the above observations are inline with what is typically observed in the literature, it is also important to verify the energy distribution across the scales of the flow. To that end, we measure the turbulent kinetic energy spectrum, which shows the expected $-5/3$ Kolmogorov scaling in the inertial subrange in figure 17. This additionally validates our model and outlines a path towards complex multicomponent flow simulations.

5. Conclusion

Let us consider a ‘good’ lattice Boltzmann setting for a single-component gas. From past experience, this would imply a two-population LBM because the second population would be ultimately needed for an adequate description of the energy, leaving aside a special case of monatomic gas. It is then possible to envision, following the rule of the conventional kinetic theory (Chapman & Cowling 1990), a valid lattice Boltzmann model for a mixture of such gases, with the total number of kinetic equations equal to $2 \times M$ for the M-component mixture since each component needs to be represented by its individual two-population LBM.

In contrast, in this paper we proposed a lattice Boltzmann framework for multicomponent mixtures of ideal gases with a more realistic number of coupled lattice Boltzmann equations. We addressed two equally important aspects. First, we proposed

a new LBM system for the Stefan–Maxwell diffusion and barodiffusion comprising M lattice Boltzmann equations. Second, we proposed a reduced, mean-field description of the mixture momentum and energy using the two-population setting. The resulting framework consists of $M + 2$ lattice Boltzmann equations (or, eventually, $M + 1$ if the strong coupling (3.66) is used) rather than $2 \times M$ as it would be if the detailed and not the mean-field approach to the energy of the mixture would have been pursued.

Special attention was devoted to the consistent thermodynamic coupling of the above two sub-systems in such a manner that the hydrodynamic limit is not compromised. The proposed framework was realized on the standard three-dimensional lattice using an extension of the compressible model of Saadat *et al.* (2019). Specific to the multicomponent problem, the interdiffusion energy flux was added in a natural way to the heat flux to recover the correct energy equation while a counter-flux was introduced to remove the spurious contribution to the Fourier law inevitably arising with the mean-field approach to the energy description. While we focused on the multicomponent case, the proposed realization is also an extension of the augmented, compressible LB model proposed by Saadat *et al.* (2019) to a general form in three dimensions, which can of course also be used for single-component flows.

The simulation of the diffusion in a ternary mixture demonstrated that the proposed LBM correctly accounts for binary interaction between species. The coupling of diffusion to hydrodynamics was assessed by computing diffusion in opposed jets and the basic compressibility features were demonstrated through the speed of sound simulation at various compositions. Finally, the simulation of the three-dimensional shear layer instability in a binary mixture with a high composition contrast indicates that the proposed method can be useful for direct numerical simulations of complex flows.

All of the above gives us grounds to believe that the proposed multicomponent framework fills the gap in the development of the LBM and is a first step towards reactive flow applications which will be the focus of our future studies.

Acknowledgements

We thank S.A. Hosseini for a discussion of the passive scalar LBM Hosseini *et al.* (2018). This work was supported by European Research Council (ERC) Advanced Grant no. 834763-PonD. Computational resources at the Swiss National Super Computing Center CSCS were provided under grant no. s897. Authors thank S. Springman and A. Togni for enabling research of N.S. at ETHZ.

Declaration of interests

The authors report no conflict of interest.

Appendix A. Kinetic models for multicomponent diffusion approximations

A.1. *Kinetic equations and hydrodynamic limit*

A variety of approximate constitutive relations for the multicomponent diffusion have been proposed in the literature, where the Stefan–Maxwell diffusion relation is substituted by a simpler surrogate expression. To that end, diffusion models such as Curtiss–Hirschfelder or mixture-averaged approximation are widely used, especially in combustion problems (see e.g. Kee *et al.* (2003); Poinsot & Veynante (2005); Giovangigli (2012); a comprehensive review can be found in Giovangigli (2015)). While the main

focus of our study is the Stefan–Maxwell diffusion model, it is interesting to see how approximate diffusion models are realized in the present setting. We start with the continuous time-space kinetic equation in the relaxation form (2.42) and modify it as follows:

$$\partial_t f_{ai} + \boldsymbol{c}_i \nabla f_{ai} = \frac{1}{\tau_a}(f_{ai}^{eq} - f_{ai}) - \Lambda_a \sum_{b=1}^{M} \frac{1}{\tau_b}(f_{bi}^{eq} - f_{bi}^{*}). \tag{A 1}$$

Here, nondimensional parameters $\Lambda_a \geq 0$ may depend on the locally conserved quantities and must satisfy the normalization

$$\sum_{a=1}^{M} \Lambda_a = 1. \tag{A 2}$$

A comparison with the previous kinetic equation (2.42) reveals a replacement of the Stefan–Maxwell source term (2.41) with a projected version thereof,

$$F_{ai} \to \tilde{F}_{ai}, \tag{A 3}$$

where

$$\tilde{F}_{ai} = \Lambda_a \sum_{b=1}^{M} \frac{1}{\tau_b}(f_{bi}^{eq} - f_{bi}^{*}). \tag{A 4}$$

On the other hand, the definitions of the equilibrium and of the quasi-equilibrium distributions remain as in § 2. Hence, it can be readily seen that the modified kinetic equations (A 1) retain both the mass and the momentum conservation for any partition Λ_a. Consequently, analysis of § 2.3 holds, and instead of the Stefan–Maxwell constitutive relation we arrive at a mixture-averaged diffusion relation

$$P\nabla X_a + (X_a - Y_a)\nabla P = -\frac{1}{\tau_a}\rho_a \delta \boldsymbol{u}_a + \Lambda_a \left(\sum_{b=1}^{M} \frac{1}{\tau_b} \rho_b \delta \boldsymbol{u}_b \right). \tag{A 5}$$

Unlike the original Stefan–Maxwell constitutive relation (2.30), (A 5) can be readily resolved to obtain the explicit expression of the diffusion flux. In order to save notation, we introduce the Stefan–Maxwell thermodynamic force $\boldsymbol{d}_a$:

$$\boldsymbol{d}_a = P\nabla X_a + (X_a - Y_a)\nabla P. \tag{A 6}$$

With this definition, the solution for (A 5) reads as

$$\rho_a \delta \boldsymbol{u}_a = -\tau_a \boldsymbol{d}_a + T_a \sum_{k=1}^{M} \tau_k \boldsymbol{d}_k, \tag{A 7}$$

where T_a is a (normalized) partition of relaxation times

$$T_a = \frac{\Lambda_a \tau_a}{\sum_{b=1}^{M} \Lambda_b \tau_b}. \tag{A 8}$$

With the momentum flux $\rho_a \boldsymbol{u}_a = \rho_a \boldsymbol{u} + \rho_a \delta \boldsymbol{u}_a$, the species equation (2.20) becomes

$$\partial_t(\rho Y_a) + \boldsymbol{\nabla} \cdot (\rho Y_a \boldsymbol{u}) - \boldsymbol{\nabla} \cdot ((1 - T_a)\tau_a \boldsymbol{d}_a) + \boldsymbol{\nabla} \cdot \left(T_a \sum_{b \neq a}^{M} \tau_b \boldsymbol{d}_b \right) = 0. \tag{A 9}$$

Upon summation over the components, it is readily verified that the species equations (A 9) satisfy the mass balance

$$\partial_t \rho + \boldsymbol{\nabla} \cdot (\rho \boldsymbol{u}) = 0. \tag{A 10}$$

Following standard terminology (Williams 1985; Poinsot & Veynante 2005; Bird *et al.* 2006; Giovangigli 2012), the last term in (A 9) is referred to as a mass correction. In the above derivation, the mass correction appears by construction as a direct implication of the momentum conservation by kinetic equations (A 1). In order to link the result (A 9) with the standard literature, we set

$$\Lambda_a^m = \left(\frac{Y_a}{\tau_a} \right) \left(\sum_{b=1}^{M} \frac{Y_b}{\tau_b} \right)^{-1}, \tag{A 11}$$

which implies in (A 8),

$$T_a^m = Y_a, \tag{A 12}$$

while (A 9) recovers the standard mixture-averaged (or Curtiss–Hirschfelder) approximation (Curtiss & Hirschfelder 1949; Kee *et al.* 2003; Poinsot & Veynante 2005; Giovangigli 2012). In order to recast it in a more familiar form, we neglect barodiffusion and introduce the mixture-averaged diffusion fluxes $\boldsymbol{j}_a^m$ (Kee *et al.* 2003):

$$\boldsymbol{j}_a^m = -(1 - Y_a)\tau_a P \boldsymbol{\nabla} X_a. \tag{A 13}$$

We note (Kee *et al.* 2003) that the mixture-averaged diffusion fluxes, in general, do not satisfy mass conservation, $\sum_{a=1}^{M} \boldsymbol{j}_a^m \neq 0$, unlike the diffusion fluxes (A 7). Substituting the Stefan–Maxwell relaxation times τ_a (2.40),

$$\tau_a = \frac{1}{R_a T \displaystyle\sum_{b \neq a}^{M} X_b / \mathcal{D}_{ab}}, \tag{A 14}$$

we obtain in (A 13),

$$\boldsymbol{j}_a^m = -\rho \left(\frac{Y_a}{X_a} \right) D_a^m \boldsymbol{\nabla} X_a, \tag{A 15}$$

where the standard mixture-averaged diffusion coefficient D_a^m of the species a is

$$D_a^m = \frac{1 - Y_a}{\displaystyle\sum_{b \neq a}^{M} X_b / \mathcal{D}_{ab}}. \tag{A 16}$$

With these definitions, the species balance equations (A 9) become

$$\partial_t(\rho Y_a) + \boldsymbol{\nabla} \cdot (\rho Y_a \boldsymbol{u}) + \boldsymbol{\nabla} \cdot \boldsymbol{j}_a^m - \boldsymbol{\nabla} \cdot \left(Y_a \sum_{b \neq a}^{M} \frac{\boldsymbol{j}_b^m}{1 - Y_b} \right) = 0. \tag{A 17}$$

Since the Curtiss–Hirschfelder diffusion equation (A 17) is a special case of the generic equation (A 9), it satisfies the mass balance, which can also be verified directly by summation over the species in (A 17).

A.2. *Lattice Boltzmann realization*

Starting with the kinetic equations (A 1), the derivation of the lattice Boltzmann scheme proceeds along the lines of § 2.5, and we present the result of this derivation. In the notation from § 2.5.3, the species lattice Boltzmann equations now read

$$f_{ai}(\boldsymbol{x}+\boldsymbol{c}_i\delta t, t+\delta t) - f_{ai}(\boldsymbol{x}, t) = 2\beta_a[f_{ai}^{eq} - f_{ai}] + \delta t(\beta_a - 1)\tilde{F}_{ai}, \tag{A 18}$$

where the difference is in the last term; instead of the expression (2.54) we now have the corresponding averaged version thereof:

$$\tilde{F}_{ai} = \Lambda_a \sum_{b=1}^{M} \frac{1}{\tau_b}[f_{bi}^{eq}(\rho_b, \boldsymbol{u}, R_bT) - f_{bi}^{*}(\rho_b, \boldsymbol{u}+\boldsymbol{V}_b, R_bT)]. \tag{A 19}$$

Consequently, the transformed diffusion velocity of the components, $\boldsymbol{V}_a$, $a = 1, \ldots, M$, are now defined by a set of linear relations:

$$\boldsymbol{V}_a - \frac{\delta t}{2}\left[-\frac{1}{\tau_a}\boldsymbol{V}_a + \Lambda_a\left(\sum_{b=1}^{M}\frac{Y_b\boldsymbol{V}_b}{Y_a\tau_b}\right)\right] = \boldsymbol{u}_a - \boldsymbol{u}. \tag{A 20}$$

Unlike its Stefan–Maxwell counterpart, (2.55), the linear system (A 20) admits an explicit solution for any number of species M:

$$\boldsymbol{V}_a = (1-\beta_a)(\boldsymbol{u}_a - \boldsymbol{u}) + \left(\frac{(1-\beta_a)\Lambda_a}{1 - \sum_{b=1}^{M}\beta_b\Lambda_b}\right)\sum_{k=1}^{M}\beta_k\left(\frac{Y_k}{Y_a}\right)(\boldsymbol{u}_k - \boldsymbol{u}), \tag{A 21}$$

where, as before in (2.51),

$$\beta_a = \frac{\delta t}{2\tau_a + \delta t}. \tag{A 22}$$

Finally, all considerations of the mixture momentum and energy as presented in § 3 remain valid without any amendments.

The present scheme for the Curtiss–Hirschfelder diffusion approximation was validated with the diffusion in the opposing jets benchmark in § 4.3; results are presented in figure 18. The LBM solution for the mole fractions of all the components as well as the scaled velocity agree well with the reference solution produced by Cantera (Goodwin *et al.* 2018). In comparison with the Stefan–Maxwell diffusion model, figure 11 also shows that Curtiss–Hirschfelder approximation is quite reliable, as should be expected in this case. It should be noted that numerical solution of the transform (2.55) required for the Stefan–Maxwell formulation does not produce any significant overheads as compared with using the corresponding explicit expression (A 21) for the mixture-averaged formulation.

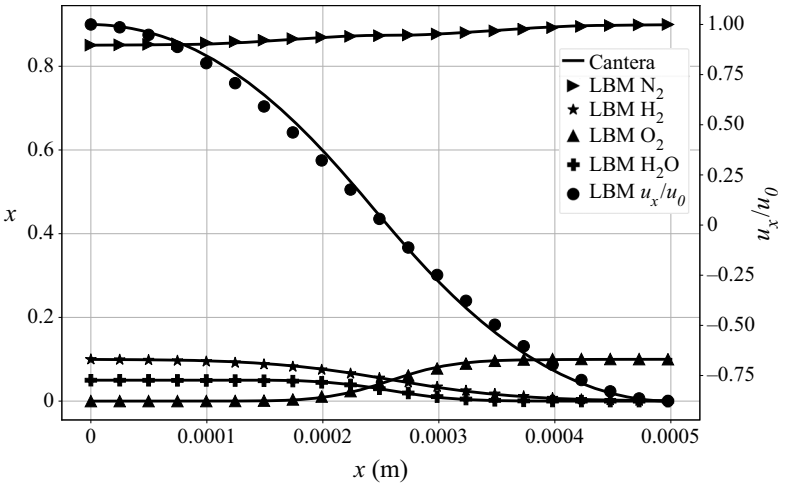

FIGURE 18. Mole fractions of H_2, N_2, O_2 and H_2O and flow velocity at stagnation line. The Curtiss–Hirschfelder diffusion formulation for the set-up of § 4.3.

A.3. *Discussion of kinetic approximations*

The structure of the kinetic system (A 1) can be made more transparent when considered in the M-dimensional space of population vectors $\boldsymbol{f}_i = (f_{1i}, \ldots, f_{Mi})^\dagger$. We recognize that the system (A 1) can be written as follows:

$$\partial_t \boldsymbol{f}_i + \boldsymbol{c}_i \cdot \nabla \boldsymbol{f}_i = \tau^{-1}(\boldsymbol{f}_i^{eq} - \boldsymbol{f}_i) - \boldsymbol{\Lambda}\tau^{-1}(\boldsymbol{f}_i^{eq} - \boldsymbol{f}_i^*), \tag{A 23}$$

where τ^{-1} is the diagonal matrix of inverse relaxation times, $\tau^{-1} = diag(\tau_1^{-1}, \ldots, \tau_M^{-1})$, and where the matrix Λ is

$$\Lambda = \begin{pmatrix} \Lambda_1 & \cdots & \Lambda_1 \\ \cdots & \cdots & \cdots \\ \Lambda_M & \cdots & \Lambda_M \end{pmatrix}. \tag{A 24}$$

Thanks to (A 2), it can be readily seen that the operator Λ (A 24) is a projector:

$$\Lambda^2 = \Lambda. \tag{A 25}$$

On the other hand, we note the multi-component representation of diffusion fluxes (Kee *et al.* 2003; Poinsot & Veynante 2005; Giovangigli 2012),

$$\rho_a \delta \boldsymbol{u}_a = \sum_{b=1}^{M} D_{ab} \boldsymbol{d}_b, \tag{A 26}$$

where the diffusion matrix D_{ab} is constructed by iteration on the Stefan–Maxwell constitutive relation (Giovangigli 2015). It is interesting to note that the use of the projection operation in the above derivation of the kinetic model for the Curtiss–Hirschfelder approximation parallels the first iteration of the diffusion matrix as described by Giovangigli (2015):

$$D_{ab}^{(1)} = -\tau_a \delta_{ab} + Y_a \tau_b. \tag{A 27}$$

Kinetic models corresponding to next-order iterations of the multi-component diffusion representation (A 26) can be considered accordingly. The specific construction of the

kinetic equation for these cases remains beyond the scope of this paper. We note that the exact multi-component diffusion matrix (A 26) is equivalent to the Stefan–Maxwell constitutive relation (Kee *et al.* 2003), and which was proposed above in the kinetic equation setting.

Finally, we note that the diffusion models discussed so far, the Stefan–Maxwell original formulation and its simplified descendants, inherit a common trait: diffusion is driven by the non-uniformity of the molar fraction X_a (and by the pressure non-uniformity). In some cases, a (generalized) Fick's diffusion approximation is used instead, where the driving force of diffusion is due to the gradient of the mass fraction ∇Y_a. In order to recover the generalized Fick's diffusion, we modify the equilibrium populations f_{ai}^{eq} (2.35) and the quasi-equilibrium populations f_{ai}^{*} (2.36) as follows:

$$f_{ai}^{eq}(\rho_a, \boldsymbol{u}, RT) = \rho_a \Psi_{c_{ix}}(u_x, RT)\Psi_{c_{iy}}(u_y, RT)\Psi_{c_{iz}}(u_z, RT), \tag{A 28}$$

$$f_{ai}^{*}(\rho_a, \boldsymbol{u}_a, RT) = \rho_a \Psi_{c_{ix}}(u_{ax}, RT)\Psi_{c_{iy}}(u_{ay}, RT)\Psi_{c_{iz}}(u_{az}, RT). \tag{A 29}$$

In other words, the equilibrium (A 28) and the quasi-equilibrium (A 29) are still represented with the product form (2.34) by choosing $\boldsymbol{\xi} = \boldsymbol{u}$ or $\boldsymbol{\xi} = \boldsymbol{u}_a$, respectively, while assigning $\zeta = RT$ in (A 28) and (A 29) instead of $\zeta = R_a T$ in (2.35) and (2.36). One can readily verify that the equilibrium (A 28) and the quasi-equilibrium (A 29) satisfy all the constraints put forward in § 2.2 except for the equilibrium pressure tensor of the species (2.18) which now becomes

$$\sum_{i=0}^{Q-1} f_{ai}^{eq} \boldsymbol{c}_i \otimes \boldsymbol{c}_i = Y_a P \boldsymbol{I} + \rho_a \boldsymbol{u} \otimes \boldsymbol{u}. \tag{A 30}$$

With this modification of the equilibrium and quasi-equilibrium populations, the kinetic system (A 1) still retains the mass and momentum conservation as before; however, the analysis of the hydrodynamic limit yields a constitutive relation with the Fick rather than the Stefan–Maxwell thermodynamic force

$$P\nabla Y_a = -\frac{1}{\tau_a}\rho_a \delta \boldsymbol{u}_a + \Lambda_a \left(\sum_{b=1}^{M} \frac{1}{\tau_b} \rho_b \delta \boldsymbol{u}_b \right). \tag{A 31}$$

The next steps of the analysis proceed with § 1, provided the thermodynamic force (A 6) is replaced by $\boldsymbol{d}_a = P\nabla Y_a$. The diffusion equation becomes

$$\partial_t(\rho Y_a) + \nabla \cdot (\rho Y_a \boldsymbol{u}) - \nabla \cdot (\rho D_a \nabla Y_a) + \nabla \cdot \left(T_a \rho \sum_{b=1}^{M} D_b \nabla Y_b \right) = 0, \tag{A 32}$$

where the diffusion coefficients $D_a = \tau_a RT$ can be computed in a variety of ways, with or without the Stefan–Maxwell binary diffusion coefficients in mind. The so-called fixed Schmidt number approximation (Poinsot & Veynante 2005; Hosseini *et al.* 2018) is obtained when the Stefan–Maxwell origin of diffusion is dropped in favour of the Schmidt number definition $Sc_a = \mu/\rho D_a$, where μ is the mixture dynamic viscosity (3.42). In order to derive the fixed Schmidt number approximation in the present context, it suffices to interpret the relaxation times (A 14) as $\tau_a = D_a/RT$, where the diffusion coefficient is evaluated as $D_a = \mu/\rho Sc_a$.

Again, the mass correction is taken into account automatically in (A 32) by construction, and is implied by momentum conservation, for any projector Λ. In particular, the choice of Λ_a as in (A 11) brings (A 32) to a canonical form

$$\partial_t Y_a + \boldsymbol{u}\cdot\nabla Y_a - \frac{1}{\rho}\nabla\cdot(\rho D_a \nabla Y_a) + \frac{1}{\rho}\nabla\cdot\left(Y_a\rho\sum_{b=1}^{M} D_b\nabla Y_b\right) = 0. \tag{A 33}$$

The lattice Boltzmann scheme is realized as in § 2, subject to a replacement of f_{ai}^{eq} and f_{ai}^{*} with (A 28) and (A 29) elsewhere in (A 18) and (A 4).

In summation, the Stefan–Maxwell constitutive relations and various approximations thereof derived in this appendix A are realized in a uniform setting of kinetic models for the species in the first place, thanks to the momentum conservation by the species sub-system. This implied mass conservation not only for the Stefan–Maxwell case but also for its approximations where mass correction becomes an integral part of the model. This is different from the passive scalar approach to kinetic models of diffusion where mass correction needs to be fixed by additional considerations (Hosseini *et al.* 2018).

Appendix B. Hydrodynamic limit of the mean-field LBM

We expand the lattice Boltzmann equations (3.21) and (3.22) in Taylor series to second order, using space component notation and summation convention:

$$\left[\delta t(\partial_t + c_{i\mu}\partial_\mu) + \frac{\delta t^2}{2}(\partial_t + c_{i\mu}\partial_\mu)^2\right] f_i = \omega(f_i^{eq} - f_i), \tag{B 1}$$

$$\left[\delta t(\partial_t + c_{i\mu}\partial_\mu) + \frac{\delta t^2}{2}(\partial_t + c_{i\mu}\partial_\mu)^2\right] g_i = \omega_1(g_i^{eq} - g_i) + (\omega-\omega_1)(g_i^{*} - g_i). \tag{B 2}$$

With a time scale $\bar{t}$ and a velocity scale $\bar{c}$, the non-dimensional parameters are introduced as follows:

$$t' = \frac{t}{\bar{t}}, \quad c'_\alpha = \frac{c_\alpha}{\bar{c}}, \quad x'_\alpha = \frac{x_\alpha}{\bar{c}\bar{t}}. \tag{B 3a–c}$$

Substituting the relations (B 3a–c) into (B 1) and (B 2), the kinetic equations in the non-dimensional form become

$$\left[\delta t'(\partial_{t'} + c'_{i\mu}\partial_{\mu'}) + \frac{\delta t'^2}{2}(\partial_{t'} + c'_{i\mu}\partial_{\mu'})^2\right] f_i = \omega(f_i^{eq} - f_i), \tag{B 4}$$

$$\left[\delta t'(\partial_{t'} + c'_{i\mu}\partial_{\mu'}) + \frac{\delta t'^2}{2}(\partial_{t'} + c'_{i\mu}\partial_{\mu'})^2\right] g_i = \omega_1(g_i^{eq} - g_i) + (\omega-\omega_1)(g_i^{*} - g_i). \tag{B 5}$$

Let us define a smallness parameter ϵ as

$$\epsilon = \delta t' = \frac{\delta t}{\bar{t}}. \tag{B 6}$$

Using the definition of ϵ and dropping the primes for ease of writing, we obtain

$$\left[\epsilon(\partial_t + c_{i\mu}\partial_\mu) + \frac{\epsilon^2}{2}(\partial_t + c_{i\mu}\partial_\mu)^2\right] f_i = \omega(f_i^{eq} - f_i), \tag{B 7}$$

$$\left[\epsilon(\partial_t + c_{i\mu}\partial_\mu) + \frac{\epsilon^2}{2}(\partial_t + c_{i\mu}\partial_\mu)^2\right] g_i = \omega_1(g_i^{eq} - g_i) + (\omega-\omega_1)(g_i^{*} - g_i). \tag{B 8}$$

Writing a power series expansion in ϵ as

$$\partial_t = \partial_t^{(1)} + \epsilon \partial_t^{(2)}, \tag{B 9}$$

$$f_i = f_i^{(0)} + \epsilon f_i^{(1)} + \epsilon^2 f_i^{(2)}, \tag{B 10}$$

$$g_i = g_i^{(0)} + \epsilon g_i^{(1)} + \epsilon^2 g_i^{(2)}, \tag{B 11}$$

$$g_i^* = g_i^{*(0)} + \epsilon g_i^{*(1)} + \epsilon^2 g_i^{*(2)}, \tag{B 12}$$

we substitute (B 9)–(B 12) into (B 7) and (B 8), and proceed with collecting terms of same order. This is standard (Chapman & Cowling 1990); for the specific case of the two-population LBM, see e.g. Karlin *et al.* (2013). At order ϵ^0, we get

$$f_i^{(0)} = f_i^{eq}, \tag{B 13}$$

$$g_i^{(0)} = g_i^{*(0)} = g_i^{eq}. \tag{B 14}$$

At order ϵ^1, upon summation over the discrete velocities, we find

$$\partial_t^{(1)} \rho + \partial_\alpha j_\alpha^{eq} = 0, \tag{B 15}$$

$$\partial_t^{(1)} j_\alpha^{eq} + \partial_\beta P_{\alpha\beta}^{eq} = 0, \tag{B 16}$$

$$\partial_t^{(1)} (\rho E) + \partial_\alpha q_\alpha^{eq} = 0. \tag{B 17}$$

Here, ρ is the density of the fluid given by the zeroth moment of the f-populations in (3.23), j_α^{eq} is the equilibrium momentum of the fluid as defined by (3.24), $P_{\alpha\beta}^{eq}$ is the equilibrium pressure tensor and q_α^{eq} is the equilibrium heat flux as defined by (3.26) and (3.28), respectively, and ρE is the total energy of the fluid calculated as the zeroth moment of g-populations using (3.25). Finally, at order ϵ^2 we arrive at

$$\partial_t^{(2)} \rho = 0, \tag{B 18}$$

$$\partial_t^{(2)} j_\alpha^{eq} + \left(\frac{1}{2} - \frac{1}{\omega}\right) \partial_\beta (\partial_t^{(1)} P_{\alpha\beta}^{eq} + \partial_\gamma Q_{\alpha\beta\gamma}^{eq}) = 0, \tag{B 19}$$

$$\partial_t^{(2)} (\rho E) + \partial_\alpha \left[\left(\frac{1}{2} - \frac{1}{\omega}\right) (\partial_t^{(1)} q_\alpha^{eq} + \partial_\beta R_{\alpha\beta}^{eq}) + \left(1 - \frac{\omega_1}{\omega}\right) q_\alpha^{*(1)} \right] = 0. \tag{B 20}$$

Here, $Q_{\alpha\beta\gamma}^{eq}$ and $R_{\alpha\beta}^{eq}$ are the third-order moment of f_i^{eq} and the second-order moment of g_i^{eq}, respectively. Their expressions are given by (3.27) and (3.29), respectively. Combining terms at both orders, we recover the following macroscopic equations:

$$\partial_t \rho + \partial_\alpha j_\alpha^{eq} = 0, \tag{B 21}$$

$$\partial_t j_\alpha^{eq} + \partial_\beta P_{\alpha\beta}^{eq} + \epsilon \left(\frac{1}{2} - \frac{1}{\omega}\right) \partial_\beta (\partial_t^{(1)} P_{\alpha\beta}^{eq} + \partial_\gamma Q_{\alpha\beta\gamma}^{eq}) = 0, \tag{B 22}$$

$$\partial_t (\rho E) + \partial_\alpha q_\alpha^{eq} + \epsilon \partial_\alpha \left[\left(\frac{1}{2} - \frac{1}{\omega}\right) (\partial_t^{(1)} q_\alpha^{eq} + \partial_\beta R_{\alpha\beta}^{eq}) + \left(1 - \frac{\omega_1}{\omega}\right) q_\alpha^{*(1)} \right] = 0, \tag{B 23}$$

where

$$\partial_t^{(1)} P_{\alpha\beta}^{eq} + \partial_\gamma Q_{\alpha\beta\gamma}^{eq} = -\frac{PR}{C_v}\partial_\gamma u_\gamma \delta_{\alpha\beta} + P(\partial_\alpha u_\beta + \partial_\beta u_\alpha), \tag{B 24}$$

$$\partial_t^{(1)} q_\alpha^{eq} + \partial_\beta R_{\alpha\beta}^{eq} = P\left(1 - \frac{C_p}{C_v}\right) u_\alpha \partial_\beta u_\beta + P u_\beta (\partial_\alpha u_\beta + \partial_\beta u_\alpha) + P \sum_{a=1}^{M} H_a \partial_\alpha Y_a + P C_p \partial_\alpha T, \tag{B 25}$$

$$q_\alpha^{*(1)} = \left(\frac{1}{\omega_1}\right)(\partial_t^{(1)} q_\alpha^{eq} + \partial_\beta R_{\alpha\beta}^{eq}) + \frac{1}{\epsilon}\left(\frac{\omega}{\omega_1}\right)(-u_\beta (P_{\alpha\beta} - P_{\alpha\beta}^{eq}) + q_\alpha^{diff} + q_\alpha^{corr}), \tag{B 26}$$

$$P_{\alpha\beta} - P_{\alpha\beta}^{eq} = \epsilon\left(-\frac{1}{\omega}\right)(\partial_t^{(1)} P_{\alpha\beta}^{eq} + \partial_\gamma Q_{\alpha\beta\gamma}^{eq}). \tag{B 27}$$

We now substitute for the moments from the expressions (B 24)–(B 27) in (B 21)–(B 23) and for the equilibrium moments from (3.23)–(3.32) to get the resulting macroscopic equations. Equation (B 21) recovers the continuity equation

$$\partial_t \rho + \partial_\alpha (\rho u_\alpha) = 0. \tag{B 28}$$

Equation (B 22) recovers the mixture momentum equation

$$\partial_t (\rho u_\alpha) + \partial_\beta (\rho u_\alpha u_\beta) + \partial_\beta \pi_{\alpha\beta} = 0, \tag{B 29}$$

with the constitutive relation for the stress tensor

$$\pi_{\alpha\beta} = P\delta_{\alpha\beta} - \mu\left(\partial_\alpha u_\beta + \partial_\beta u_\alpha - \frac{2}{D}(\partial_\mu u_\mu)\delta_{\alpha\beta}\right) - \varsigma(\partial_\mu u_\mu)\delta_{\alpha\beta}. \tag{B 30}$$

The dynamic viscosity μ and the bulk viscosity ς are related to the relaxation coefficient ω by (3.42) and (3.43), respectively. Finally, (B 23) recovers the mixture energy equation

$$\partial_t (\rho E) + \partial_\alpha (\rho E u_\alpha) + \partial_\alpha (\pi_{\alpha\beta} u_\beta) + \partial_\alpha q_\alpha = 0, \tag{B 31}$$

where the heat flux $\boldsymbol{q}$ has the following form:

$$q_\alpha = -\lambda \partial_\alpha T - \epsilon P\left(\frac{1}{\omega_1} - \frac{1}{2}\right)\sum_{a=1}^{M} H_a \partial_\alpha Y_a + \left(\frac{\omega}{\omega_1} - 1\right) q_\alpha^{corr} + \left(\frac{\omega}{\omega_1} - 1\right) q_\alpha^{diff}, \tag{B 32}$$

with the thermal conductivity λ defined by (3.46). We now choose q_α^{corr} to cancel the spurious second term containing the gradient of Y_a:

$$q_\alpha^{corr} = \frac{1}{2}\left(\frac{\omega_1 - 2}{\omega_1 - \omega}\right)\epsilon P \sum_{a=1}^{M} H_a \partial_\alpha Y_a. \tag{B 33}$$

This is equivalent to (3.36). Finally, the interdiffusion energy flux is introduced by choosing the last term $\boldsymbol{q}^{diff}$ in (B 32) as

$$q_\alpha^{diff} = \left(\frac{\omega_1}{\omega - \omega_1}\right)\rho \sum_{a=1}^{M} H_a Y_a V_{a\alpha}, \tag{B 34}$$

which is equivalent to (3.35). Substituting (B 33) and (B 34) into (B 32), we get the heat flux $\boldsymbol{q}$ in the energy equation (B 31) as a combination of the Fourier law and the

interdiffusion energy flux due to diffusion of the species (Williams 1985; Bird *et al.* 2006):

$$q_\alpha = -\lambda \partial_\alpha T + \rho \sum_{a=1}^{M} H_a Y_a V_{a\alpha}. \tag{B 35}$$

Appendix C. Thermodynamic data for benchmarks

Data useful for reproducing the benchmarks in § 4 is provided here for reference. The data source is the publicly accessible GRI-Mech 3.0 mechanism (Smith *et al.* 1999) and it is calculated by the open source code Cantera (Goodwin *et al.* 2018) at a temperature of 300 K and at a pressure of 1 atm. The symbol $\mathcal{D}_{a-b}$ represents the pairwise Stefan–Maxwell mass diffusivity between the species a and b.

C.1. *Diffusion in a ternary gas mixture, § 4.2*

Property \ Species	H_2	Ar	CH_4
m_a [g mol^{-1}]	2.01588	39.948	16.0428
μ [kg m^{-1} s^{-1}]	9.00003×10^{-6}	2.31418×10^{-5}	1.14289×10^{-5}
λ [W m^{-1} K^{-1}]	0.186929	0.0180602	0.0358402
C_p [J kmol^{-1} K^{-1}]	28850.8	20786.2	35760.5

$$\left.\begin{aligned} \mathcal{D}_{H_2\text{–}Ar} &= 8.14543 \times 10^{-5}\ \mathrm{m^2\ s^{-1}} \\ \mathcal{D}_{H_2\text{–}CH_4} &= 7.37433 \times 10^{-5}\ \mathrm{m^2\ s^{-1}} \\ \mathcal{D}_{Ar\text{–}CH_4} &= 2.17321 \times 10^{-5}\ \mathrm{m^2\ s^{-1}} \end{aligned}\right\}. \tag{C 1}$$

C.2. *Diffusion in opposed jets, § 4.3*

Property \ Species	N_2	H_2	O_2	H_2O
m_a [g mol^{-1}]	28.0135	2.01588	31.9988	18.0153
μ [kg m^{-1} s^{-1}]	1.80955×10^{-5}	9.00003×10^{-6}	2.06307×10^{-5}	1.00761×10^{-5}
λ [W m^{-1} K^{-1}]	0.026478	0.186929	0.0265397	0.0255707
C_p [J kmol^{-1} K^{-1}]	29075.5	28850.8	29388.1	33596.4

$$\left.\begin{aligned} \mathcal{D}_{N_2\text{–}H_2} &= 7.79236 \times 10^{-5}\ \mathrm{m^2\ s^{-1}} \\ \mathcal{D}_{N_2\text{–}O_2} &= 2.08575 \times 10^{-5}\ \mathrm{m^2\ s^{-1}} \\ \mathcal{D}_{N_2\text{–}H_2O} &= 2.27013 \times 10^{-5}\ \mathrm{m^2\ s^{-1}} \\ \mathcal{D}_{H_2\text{–}O_2} &= 8.07143 \times 10^{-5}\ \mathrm{m^2\ s^{-1}} \\ \mathcal{D}_{H_2\text{–}H_2O} &= 8.56433 \times 10^{-5}\ \mathrm{m^2\ s^{-1}} \\ \mathcal{D}_{O_2\text{–}H_2O} &= 8.07143 \times 10^{-5}\ \mathrm{m^2\ s^{-1}} \end{aligned}\right\}. \tag{C 2}$$

C.3. *Speed of sound, § 4.4*

Property \ Species	H_2	Ar	CH_4	C_3H_8
m_a [g mol^{-1}]	2.01588	39.948	16.0428	44.0965
μ [kg m^{-1} s^{-1}]	9.00003×10^{-6}	2.31418×10^{-5}	1.14289×10^{-5}	8.23526×10^{-6}
λ [W m^{-1} K^{-1}]	0.186929	0.0180602	0.0358402	0.0183989
C_p [J kmol^{-1} K^{-1}]	28850.8	20786.2	35760.5	73950

$$\left.\begin{aligned} \mathcal{D}_{H_2\text{–}Ar} &= 8.14543 \times 10^{-5}\ \mathrm{m^2\ s^{-1}} \\ \mathcal{D}_{H_2\text{–}CH_4} &= 7.37433 \times 10^{-5}\ \mathrm{m^2\ s^{-1}} \\ \mathcal{D}_{Ar\text{–}CH_4} &= 2.17321 \times 10^{-5}\ \mathrm{m^2\ s^{-1}} \\ \mathcal{D}_{H_2\text{–}C_3H_8} &= 4.68396 \times 10^{-5}\ \mathrm{m^2\ s^{-1}} \\ \mathcal{D}_{Ar\text{–}C_3H_8} &= 1.03862 \times 10^{-5}\ \mathrm{m^2\ s^{-1}} \end{aligned}\right\}. \tag{C 3}$$

C.4. *Kelvin–Helmholtz instability, § 4.5*

Property \ Species	N_2	H_2O
m_a [g mol^{-1}]	28.0135	18.0153
μ [kg m^{-1} s^{-1}]	1.80955×10^{-5}	1.00761×10^{-5}
λ [W m^{-1} K^{-1}]	0.026478	0.0255707
C_p [J kmol^{-1} K^{-1}]	29075.5	33596.4

$$\mathcal{D}_{N_2\text{–}H_2O} = 2.27013 \times 10^{-5}\ \mathrm{m^2\ s^{-1}}. \tag{C 4}$$

REFERENCES

Ansumali, S., Arcidiacono, S., Chikatamarla, S. S., Prasianakis, N. I., Gorban, A. N. & Karlin, I. V. 2007 Quasi-equilibrium lattice Boltzmann method. *Eur. Phys. J.* B **56**, 135–139.

Arcidiacono, S., Karlin, I. V., Mantzaras, J. & Frouzakis, C. E. 2007 Lattice Boltzmann model for the simulation of multicomponent mixtures. *Phys. Rev.* E **76**, 046703.

Arnold, K. R. & Toor, H. L. 1967 Unsteady diffusion in ternary gas mixtures. *AIChE J.* **13** (5), 909–914.

Bird, R. B., Stewart, W. E. & Lightfoot, E. N. 2006 *Transport Phenomena*, Wiley International edn. Wiley.

Chai, Z., Guo, X., Wang, L. & Shi, B. 2019 Maxwell–Stefan-theory-based lattice Boltzmann model for diffusion in multicomponent mixtures. *Phys. Rev.* E **99**, 023312.

Chapman, S. T. & Cowling, T. G. 1990 *The Mathematical Theory of Non-Uniform Gases: An Account of the Kinetic Theory of Viscosity, Thermal Conduction and Diffusion in Gases*, Cambridge Mathematical Library. Cambridge University Press.

Chiavazzo, E., Karlin, I. V., Gorban, A. N. & Boulouchos, K. 2009 Combustion simulation via lattice Boltzmann and reduced chemical kinetics. *J. Stat. Mech.* **2009** (6), P06013.

Curtiss, C. F. & Hirschfelder, J. O. 1949 Transport properties of multicomponent gas mixtures. *J. Chem. Phys.* **17**, 550–555.

DORSCHNER, B., BÖSCH, F., CHIKATAMARLA, S. S., BOULOUCHOS, K. & KARLIN, I. V. 2016 Entropic multi-relaxation time lattice Boltzmann model for complex flows. *J. Fluid Mech.* **801**, 623–651.

DORSCHNER, B., BÖSCH, F. & KARLIN, I. V. 2018 Particles on demand for kinetic theory. *Phys. Rev. Lett.* **121** (13), 130602.

DORSCHNER, B., CHIKATAMARLA, S. S. & KARLIN, I. V. 2017 Transitional flows with the entropic lattice Boltzmann method. *J. Fluid Mech.* **824**, 388–412.

DUNCAN, J. B. & TOOR, H. L. 1962 An experimental study of three component gas diffusion. *AIChE J.* **8** (1), 38–41.

FENG, Y., TAYYAB, M. & BOIVIN, P. 2018 A Lattice-Boltzmann model for low-Mach reactive flows. *Combust. Flame* **196**, 249–254.

FRAPOLLI, N., CHIKATAMARLA, S. S. & KARLIN, I. V. 2015 Entropic lattice Boltzmann model for compressible flows. *Phys. Rev.* E **92**, 061301.

FRAPOLLI, N., CHIKATAMARLA, S. S. & KARLIN, I. V. 2016*a* Entropic lattice Boltzmann model for gas dynamics: theory, boundary conditions, and implementation. *Phys. Rev.* E **93** (6), 063302.

FRAPOLLI, N., CHIKATAMARLA, S. S. & KARLIN, I. V. 2016*b* Lattice kinetic theory in a comoving Galilean reference frame. *Phys. Rev. Lett.* **117** (1), 010604.

FRAPOLLI, N., CHIKATAMARLA, S. S. & KARLIN, I. V. 2018 Entropic lattice Boltzmann simulation of thermal convective turbulence. *Comput. Fluids* **175**, 2–19.

FRAPOLLI, N., CHIKATAMARLA, S. S. & KARLIN, I. V. 2020 Theory, analysis, and applications of the entropic lattice Boltzmann model for compressible flows. *Entropy* **22** (3), 370.

GAN, Y., XU, A., ZHANG, G., ZHANG, Y. & SUCCI, S. 2018 Discrete Boltzmann trans-scale modeling of high-speed compressible flows. *Phys. Rev.* E **97**, 053312.

GIOVANGIGLI, V. 2012 *Multicomponent Flow Modeling*. Birkhäuser.

GIOVANGIGLI, V. 2015 Multicomponent transport in laminar flames. *Proc. Combust. Inst.* **35**, 625–637.

GOODWIN, D. G., SPETH, R. L., MOFFAT, H. K. & WEBER, B. W. 2018 Cantera: an object-oriented software toolkit for chemical kinetics, thermodynamics, and transport processes. Version 2.4.0.

GORBAN, A. N. & KARLIN, I. V. 1994 General approach to constructing models of the Boltzmann equation. *Physica* A **206** (3–4), 401–420.

GRAD, H. 1949 On the kinetic theory of rarefied gases. *Commun. Pure Appl. Maths* **2** (4), 331–407.

GUO, Z., ZHENG, C., SHI, B. & ZHAO, T. S. 2007 Thermal lattice Boltzmann equation for low Mach number flows: decoupling model. *Phys. Rev.* E **75** (3), 036704.

HE, X., CHEN, S. & DOOLEN, G. D. 1998 A novel thermal model for the lattice Boltzmann method in incompressible limit. *J. Comput. Phys.* **146** (1), 282–300.

HIGUERA, F. J. & JIMÉNEZ, J. 1989 Boltzmann approach to lattice gas simulations. *Europhys. Lett.* **9** (7), 663–668.

HIGUERA, F. J., SUCCI, S. & BENZI, R. 1989 Lattice gas dynamics with enhanced collisions. *Europhys. Lett.* **9** (4), 345–349.

HOSSEINI, S. A., DARABIHA, N. & THEVENIN, D. 2018 Mass-conserving advection diffusion lattice Boltzmann model for multi-species reacting flows. *Physica* A **499**, 40–57.

HOSSEINI, S. A., ESHGHINEJADFARD, A., DARABIHA, N. & THÉVENIN, D. 2020 Weakly compressible lattice Boltzmann simulations of reacting flows with detailed thermo-chemical models. *Comput. Maths Applics.* **79**, 141–158.

HOSSEINI, S. A., SAFARI, H., DARABIHA, N., THÉVENIN, D. & KRAFCZYK, M. 2019 Hybrid lattice Boltzmann - finite difference model for low Mach number combustion simulation. *Combust. Flame* **209**, 394–404.

HSING, I.-M. & FUTERKO, P. 2000 Two-dimensional simulation of water transport in polymer electrolyte fuel cells. *Chem. Engng Sci.* **55** (19), 4209–4218.

KARLIN, I. & ASINARI, P. 2010 Factorization symmetry in the lattice Boltzmann method. *Physica* A **389** (8), 1530–1548.

KARLIN, I. V., SICHAU, D. & CHIKATAMARLA, S. S. 2013 Consistent two-population lattice Boltzmann model for thermal flows. *Phys. Rev.* E **88**, 063310.

KEE, R. J., COLTRIN, M. E. & GLARBORG, P. 2003 *Chemically Reacting Flow: Theory and Practice*. Wiley.

KRISHNA, R. & VAN BATEN, J. M. 2005 Diffusion of alkane mixtures in zeolites: validating the Maxwell–Stefan formulation using MD simulations. *J. Phys. Chem.* B **109** (13), 6386–6396.

KRISHNA, R. & WESSELINGH, J. A. 1997 Review article number 50 - the Maxwell–Stefan approach to mass transfer. *Chem. Engng Sci.* **52** (6), 861–911.

KRÜGER, T., KUSUMAATMAJA, H., KUZMIN, A., SHARDT, O., SILVA, G. & VIGGEN, E. M. 2017 *The Lattice Boltzmann Method*. Springer International Publishing.

LEEP, L. J., DUTTON, J. C. & BURR, R. F. 1993 Three-dimensional simulations of compressible mixing layers: visualizations and statistical analysis. *AIAA J.* **31** (11), 2039–2046.

LIN, C. & LUO, K. H. 2018 MRT discrete Boltzmann method for compressible exothermic reactive flows. *Comput. Fluids* **166**, 176–183.

LINDSTROM, M. & WETTON, B. 2017 A comparison of Fick and Maxwell–Stefan diffusion formulations in PEMFC gas diffusion layers. *Heat Mass Transfer* **53** (1), 205–212.

MATHUR, S., TONDON, P. K. & SAXENA, S. C. 1967 Thermal conductivity of binary, ternary and quaternary mixtures of rare gases. *Mol. Phys.* **12** (6), 569–579.

MAZLOOMI, A. M., CHIKATAMARLA, S. S. & KARLIN, I. V. 2015 Entropic lattice Boltzmann method for multiphase flows. *Phys. Rev. Lett.* **114** (17), 174502.

MAZLOOMI, A. M., CHIKATAMARLA, S. S. & KARLIN, I. V. 2017 Drops bouncing off macro-textured superhydrophobic surfaces. *J. Fluid Mech.* **824**, 866–885.

MONTEMORE, M. M., MONTESSORI, A., SUCCI, S., BARROO, C., FALCUCCI, G., BELL, D. C. & KAXIRAS, E. 2017 Effect of nanoscale flows on the surface structure of nanoporous catalysts. *J. Chem. Phys.* **146** (21), 214703.

MONTESSORI, A., PRESTININZI, P., LA ROCCA, M., FALCUCCI, G., SUCCI, S. & KAXIRAS, E. 2016 Effects of Knudsen diffusivity on the effective reactivity of nanoporous catalyst media. *J. Comput. Sci.* **17**, 377–383.

POINSOT, T. & VEYNANTE, D. 2005 *Theoretical and Numerical Combustion*. R.T. Edwards, Inc.

SAADAT, M. H., BÖSCH, F. & KARLIN, I. V. 2019 Lattice Boltzmann model for compressible flows on standard lattices: variable Prandtl number and adiabatic exponent. *Phys. Rev.* E **99**, 013306.

SAN, O. & MAULIK, R. 2018 Stratified Kelvin–Helmholtz turbulence of compressible shear flows. *Nonlinear Process. Geophys.* **25** (2), 457–476.

SHAN, X., YUAN, X.-F. & CHEN, H. 2006 Kinetic theory representation of hydrodynamics: a way beyond the Navier–Stokes equation. *J. Fluid Mech.* **550**, 413–441.

SHARMA, K. V., STRAKA, R. & TAVARES, F. W. 2020 Current status of lattice Boltzmann methods applied to aerodynamic, aeroacoustic, and thermal flows. *Prog. Aerosp. Sci.* **115**, 100616.

SMITH, G. P., GOLDEN, D. M., FRENKLACH, M., MORIARTY, N. W., EITENEER, B., GOLDENBERG, M., BOWMAN, C. T., HANSON, R. K., SONG, S., GARDINER, W. C. JR., *et al*. 1999 GRI-MECH 3.0. Available at: http://www.me.berkeley.edu/gri_mech/.

STOCKIE, J. M., PROMISLOW, K. & WETTON, B. R. 2003 A finite volume method for multicomponent gas transport in a porous fuel cell electrode. *Intl J. Numer. Meth. Fluids* **41** (6), 577–599.

SUCCI, S. 2018 *The Lattice Boltzmann Equation: For Complex States of Flowing Matter*. Oxford University Press.

SUWANWARANGKUL, R., CROISET, E., FOWLER, M. W., DOUGLAS, P. L., ENTCHEV, E. & DOUGLAS, M. A. 2003 Performance comparison of Ficks, dusty-gas and Stefan–Maxwell models to predict the concentration overpotential of a SOFC anode. *J. Power Sources* **122** (1), 9–18.

TAYYAB, M., ZHAO, S., FENG, Y. & BOIVIN, P. 2020 Hybrid regularized Lattice-Boltzmann modelling of premixed and non-premixed combustion processes. *Combust. Flame* **211**, 173–184.

THAMPI, S. P., ANSUMALI, S., ADHIKARI, R. & SUCCI, S. 2013 Isotropic discrete Laplacian operators from lattice hydrodynamics. *J. Comput. Phys.* **234**, 1–7.

TOOR, H. L. 1957 Diffusion in three component gas mixtures. *AIChE J.* **3** (2), 198–207.

VIENNE, L., MARIÉ, S. & GRASSO, F. 2019 Lattice Boltzmann method for miscible gases: a forcing-term approach. *Phys. Rev.* E **100**, 023309.

WHEELER, D. R. & NEWMAN, J. 2004 Molecular dynamics simulations of multicomponent diffusion. 1. Equilibrium method. *J. Phys. Chem.* B **108** (47), 18353–18361.

WILKE, C. R. 1950 A viscosity equation for gas mixtures. *J. Chem. Phys.* **18** (4), 517–519.

WILLIAMS, F. A. 1985 *Combustion Theory: The Fundamental Theory of Chemically Reacting Flow Systems*. Benjamin/Cummings.

WÖHRWAG, M., SEMPREBON, C., MAZLOOMI, A. M., KARLIN, I. & KUSUMAATMAJA, H. 2018 Ternary free-energy entropic lattice Boltzmann model with a high density ratio. *Phys. Rev. Lett.* **120** (23), 234501.

YAKABE, H., HISHINUMA, M., URATANI, M., MATSUZAKI, Y. & YASUDA, I. 2000 Evaluation and modeling of performance of anode-supported solid oxide fuel cell. *J. Power Sources* **86** (1), 423–431.

YAN, B., XU, A. G., ZHANG, G. C., YING, Y. J. & LI, H. 2013 Lattice Boltzmann model for combustion and detonation. *Front. Phys.* **8**, 94–110.